

Gravitational wave sources in our Galactic backyard: LISA predictions for BH and NS binaries

T. WAGG ^{1,2} F. BROEKGAARDEN ¹ S. E. DE MINK ^{2,3,1} N. FRANKEL ⁴ L.A.C. VAN SON ^{1,3,2} AND S. JUSTHAM ^{5,3}

¹Center for Astrophysics — Harvard & Smithsonian, 60 Garden Street, Cambridge, MA 02138, USA

²Max-Planck-Institut für Astrophysik, Karl-Schwarzschild-Straße 1, 85741 Garching, Germany

³Anton Pannekoek Institute for Astronomy & Grappa, University of Amsterdam, Postbus 94249, 1090 GE Amsterdam, The Netherlands

⁴Max Planck Institute for Astronomy, Königstuhl 17, D-69117 Heidelberg, Germany

⁵School of Astronomy & Space Science, University of the Chinese Academy of Sciences, Beijing 100012, China

(Received June 17, 2021)

ABSTRACT

...

...

...

...

...

...

...

...

...

...

...

...

...

...

...

...

...

...

...

...

...

Keywords: LISA, black hole, neutron star, binary

1. INTRODUCTION

Since the first direct observation of gravitational waves by the LIGO scientific collaboration in 2015 (Abbott et al. 2016), the number of black hole (BH) and neutron star (NS) binaries observed by ground-based gravitational-wave detectors has rapidly grown (Abbott et al. 2019, 2020b), offering exciting insights into the formation, lives and deaths of massive binary stars (e.g. Abbott et al. 2021).

The Laser Interferometer Space Antenna (LISA, Amaro-Seoane et al. 2017) will provide observations in an entirely new regime of gravitational waves. LISA will observe at lower frequencies than ground-based detectors ($10^{-5} \lesssim f/\text{Hz} \lesssim 10^{-1}$) and so will enable the study of sources that are undetectable with ground-based detectors such as the mergers of supermassive black holes and extreme mass ratio inspirals (e.g. Begelman et al. 1980; Klein et al. 2016). Moreover, this frequency regime is also of interest for the detection of local stellar mass binaries during their inspiral phase. This means that

LISA will be able to detect, and possibly localise a binary on the sky, many years in advance of the merger, which presents an opportunity for both multimessenger detections to search for electromagnetic counterparts and multiband detections that would better constrain binary characteristics (e.g. Sesana 2016; Gerosa et al. 2019). In addition, LISA will be able to measure the eccentricities of double compact objects (DCO) that may yield further constraints on binary evolution, differentiate between formation channels and distinguish between DCO types (e.g. Nelemans et al. 2001; Breivik et al. 2016; Antonini et al. 2017; Rodriguez et al. 2018). The maximum distance at which stellar mass sources in LISA are detectable is significantly lower than in ground-based detectors since the gravitational wave signal is weaker during the inspiral phase than at the merger. This means that LISA stellar mass sources can only be detected in local galaxies, with the majority residing in the Milky Way. Therefore, these sources could be used as a

probe for our galaxy’s history and evolution (e.g. Korol et al. 2019).

Traditionally, investigations into detecting stellar mass sources with LISA focus on double white dwarf (WDWD) binaries (Nelemans et al. 2001; Ruiter et al. 2010; Yu & Jeffery 2010; Nissanke et al. 2012; Korol et al. 2017; Lamberts et al. 2018). More recently, interest has grown in the detection of NS and BH binaries. Although they are rare, LISA detections of these sources could be useful for learning more about the evolution and endpoints of massive stars. In this paper we focus on NS and BH binaries.

For the purposes of this investigation, we consider the classical isolated binary evolution channel (e.g. Tutukov & Yungelson 1973, 1993; Smarr & Blandford 1976; Srinivasan 1989; Kalogera et al. 2007; Belczynski et al. 2016) in which compact objects are formed through common envelope ejection or highly non-conservative mass transfer (Heuvel 2011). There are however several alternative proposed formation channels including: dynamical formation in dense star clusters (e.g. Sigurdsson & Hernquist 1993; Portegies Zwart & McMillan 2000; Miller & Lauburg 2009; Rodriguez et al. 2015) and (active) galactic nuclei discs (e.g. Morris 1993; Antonini & Rasio 2016; McKernan et al. 2020), isolated hierarchical triple evolution involving Kozai-Lidov oscillations (e.g. Stephan et al. 2016; Silsbee & Tremaine 2017; Antonini et al. 2017) and chemically homogenous evolution through efficient rotational mixing (e.g. de Mink et al. 2009; de Mink & Mandel 2016; Marchant et al. 2016; du Buisson et al. 2020).

Galactic double neutron star (NSNS) binaries have been observed with electromagnetic signals for several decades (e.g. Hulse & Taylor 1975; Tauris et al. 2017; Vigna-Gómez et al. 2018) and more recently the mergers of NSNS binaries with ground-based gravitational wave detectors have been detected (e.g. Abbott et al. 2017). The detection of a NSNS in LISA in which at least one NS is a pulsar could potentially connect these two populations if the binary is close to merging, as the binary could be observed from inspiral to merger. NSNS binaries are useful sources for understanding the origin of r-process elements (e.g. Eichler et al. 1989) as well as the electromagnetic counterparts to gravitational wave signal such as kilonovae (e.g. Metzger 2017), short gamma-ray bursts (e.g. Gompertz et al. 2020), radio emission (e.g. Hotokezaka et al. 2016) and neutrinos (e.g. Kyutoku et al. 2018).

Double black hole (BHBH) binaries in the Milky Way present a greater observational challenge. To date, no BH has been observed to be in a binary with another compact object in the Milky Way and so LISA could pro-

vide the first detection of a Galactic BHBH binary. The only confirmed BHs in our galaxy have been discovered as components of X-ray binaries with companion stars (e.g. Bolton 1972; Webster & Murdin 1972). This sample of BHs has masses mainly constrained between 5 and $10 M_{\odot}$ (Corral-Santana et al. 2016), a stark contrast to the more massive BHs observed with LIGO/Virgo that tend to have masses concentrated around $30 M_{\odot}$ (Abbott et al. 2020b). These observations suggest the presence of a lower mass gap (from 2-5 M_{\odot}) in which no black holes or neutron stars are observed (Özel et al. 2010; Farr et al. 2011) but its existence remains an open question (e.g. Kreidberg et al. 2012). Recently there has also been increased discussion over the maximum BH mass in our galaxy, with the claims of a $70 M_{\odot}$ BH (Liu et al. 2019) which has subsequently been challenged (El-Badry & Quataert 2020; Abdul-Masih et al. 2020; Shenar et al. 2020; Eldridge et al. 2020) and revised measurements of the mass of Cygnus X-1 (Miller-Jones et al. 2021). A sample of BHBHs detected with LISA could possibly help to constrain the stellar mass BH mass distribution.

One particularly interesting and elusive gravitational wave source is a black hole neutron star binary (BHNS). Of all the events detected by ground-based detectors, none can be confidently attributed to the merger of a black hole and a neutron star, though several events such as GW190425 and GW190814 have not been ruled out as a BHNS merger (Abbott et al. 2020a,c). Predictions for the merger rate of BHNSs range across three orders of magnitude (e.g. Abadie et al. 2010; Broekgaarden et al. 2021) so the number of detections in LISA will be important in reducing this uncertainty, thereby refining our understanding of the remnants and evolution of massive stars. These binaries are expected to have electromagnetic counterparts that can be studied in the same way as NSNSs. A distinctly exciting possibility is the detection of a pulsar–BH system or millisecond pulsar–BH system (Narayan et al. 1991). These systems could be observed not only by gravitational wave detectors, but also radio telescopes such as MeerKAT and SKA, which will help to constrain uncertain binary evolution processes (e.g. Pfahl et al. 2005; Chattopadhyay et al. 2020).

The detection of DCOs with LISA has been investigated in several previous studies, yet studies that focus on BHBH, BHNS and NSNS binaries, as opposed to the numerous WDWD population, are still uncommon. Earlier work has used a variety of population synthesis codes, Milky Way models and LISA specifications, resulting in a wide range of predictions (Nelemans et al. 2001; Liu 2009; Belczynski et al. 2010a; Liu & Zhang

2014; Lamberts et al. 2019; Lau et al. 2020; Breivik et al. 2020; Sesana et al. 2020).

We build upon previous efforts but with several important improvements. We explore the effect of varying binary physics assumptions by repeating our analysis for 20 different models and comparing the effect on the detection rate and distributions of source parameters. We use a model for the Milky Way that is dependent on the chemical enrichment history and calibrated on the latest APOGEE survey (Majewski et al. 2017; Frankel et al. 2018). We provide a full treatment of the eccentricity of detectable sources both for the inspiral evolution as well as gravitational wave signal during the LISA mission. Moreover, our binary population synthesis simulation is the most extensive of its kind to date, with over a billion simulated massive binaries evolved to produce the DCO populations used in this work (Broekgaarden et al. 2021). We find that this large number of simulations is important to reduce the sampling noise. In addition, we use the adaptive sampling algorithm STROOPWAFEL (Broekgaarden et al. 2019) to further reduce this sampling noise.

In this paper, we present predictions of the detection rate and distribution of binary properties (masses, frequency, eccentricity, distance, merger time) of BHBH, BHNS and NSNS binaries formed through isolated binary evolution in the Milky Way. We explore the effect of varying physical assumptions in our population synthesis model on our results as well as discuss the effect of extending the LISA mission length and the possibility of distinguishing detections.

All data produced in this study is publicly available on Zenodo ¹ as is the population used in our simulations ². We make all code used to produce our results available in a Github repository ³. In addition, the repository contains step-by-step Jupyter notebooks that explain how to reproduce and change each figure in the paper. In a companion paper we present **LEGWORK**⁴, a python package designed for making predictions for the detection of sources with LISA, which we use in this work.

Our paper is structured as follows. In Section 2, we describe our methods for synthesising a population of binaries, the variations of physical assumptions that we consider, how we simulate the Milky Way distribution of DCOs and our methods for calculating a detection

rate for LISA. We present our main results in Section 3, analysing our findings for each DCO type and variation of physical assumptions. In Section 4 we discuss these results. In Section 5, we compare and contrast our methods and findings to previous work and finish with our conclusions in Section 6.

2. METHOD

To produce predictions for the DCOs that are detectable with LISA, we synthesise a population of DCOs using the population synthesis methods described in Section 2.1. In order to obtain value for the uncertainty on the expected detection rates, we place this sample of DCOS in many different Monte Carlo sampled instances of the Milky Way, the model for which is described in Section 2.2. We evolve the orbit of each DCO in a Milky Way instance up to the LISA mission and calculate the detection rate for that instance using the methods presented in Section 2.3.

2.1. *Binary population synthesis*

We use a population of binaries recently presented in Broekgaarden et al. (2021) and Broekgaarden et al. (in prep). This population is synthesised using the rapid population synthesis code COMPAS⁵ (Stevenson et al. 2017; Vigna-Gómez et al. 2018; Stevenson et al. 2019). COMPAS follows the approach of the pioneering population synthesis code BSE (Hurley et al. 2000, 2002) and uses fitting formula and rapid algorithms to efficiently predict the final fate of millions of binary systems. The code is open source and documented in the papers listed above and the on-line documentation. An extensive method paper is forthcoming (Team COMPAS: J. Riley et al. (in prep)). We summarize the main assumptions and settings relevant for this work in the following sections.

2.1.1. *Initial conditions*

One million binaries are simulated for 50 metallicity bins equally spaced in log space between $Z \in [0.0001, 0.022]$, where Z is the mass fraction of heavy elements. These bins span the allowed metallicities range for the original fitting formulae on which COMPAS is based (Hurley et al. 2000). This is repeated for 19 physics variations (see Section 2.1.3) and so in total over a billion binaries were simulated.

Each binary is sampled from initial distributions for the primary and secondary masses as well as the separation. The primary mass, that is the mass of the initially more massive star, is restricted to $m_1 \in [5, 150] M_\odot$,

¹<https://zenodo.org/record/4699713>

²<https://zenodo.org/record/4574727>

³<https://github.com/TomWagg/detecting-DCOs-in-LISA>

⁴<https://legwork.readthedocs.io>

⁵<https://compas.science>

which spans the range of interest for NS and BH formation in binary systems, and drawn from the [Kroupa \(2001\)](#) initial mass function (IMF), $p(m_1) \propto m_1^{-2.3}$. The secondary mass is drawn using the mass ratio of the binary, which we assume to be uniform on $[0, 1]$, therefore $p(q) = 1$ (consistent e.g. with [Sana et al. 2012](#)). We additionally restrict $m_2 \geq 0.1 M_\odot$, since this is approximately the minimal mass for a main sequence star. We assume that the initial separation follows a flat in the log distribution with $p(a_i) \propto 1/a_i$ and $a_i \in [0.01, 1000] \text{ AU}$ ([Öpik 1924; Abt 1983](#)). We assume that all binaries are circular at birth to reduce the dimensions of initial parameters. Since we focus on post-interaction binaries which will have circularised during mass transfer this is a reasonable assumption and is likely not critical for predicting detection rates ([Hurley et al. 2002; de Mink & Belczynski 2015](#)). In addition, we apply the adaptive importance sampling algorithm STROOPWAFEL ([Broekgaarden et al. 2019](#)) to improve the yield of our sample. This algorithm increases the prevalence of target DCOs (BHBHs, BHNSs and NSNSs in this case) in the sample and assigns each a weight, w , which represents the probability of drawing it without STROOPWAFEL in effect.

For each metallicity Z , we thus have a sample of binaries, each with a set of parameters

$$\mathbf{b}_{Z,i} = \{m_1, m_2, a_{\text{DCO}}, e_{\text{DCO}}, t_{\text{evolve}}, t_{\text{inspiral}}, w\}, \quad (1)$$

for $i = 1, 2, \dots, N_{\text{binary}}$, where m_1 and m_2 are the primary and secondary masses, a_{DCO} and e_{DCO} are the semi-major axis and eccentricity at the moment of double compact object (DCO) formation, t_{evolve} is the time between the binary's zero-age main sequence and DCO formation, t_{inspiral} is the time between DCO formation (that is immediately after the second supernova in the system) and gravitational wave merger, w is the adaptive importance sampling weight assigned by STROOPWAFEL. We sample from these sets of parameters when creating synthetic galaxies.

2.1.2. Physical assumptions in fiducial model

In this section we briefly summarise the main physical assumptions in our fiducial model. For more details see [Broekgaarden et al. \(2021\)](#).

Stellar Evolution: To follow the evolution of massive stars, COMPAS relies on fitting formula by [Hurley et al. \(2000\)](#) to detailed single star models by [Pols et al. \(1998\)](#). COMPAS implements stellar wind mass loss using the prescriptions from [Belczynski et al. \(2010b\)](#) and models the evolution of stars that lose or gain mass closely following the algorithms originally described in [Tout et al. \(1996\)](#) and [Hurley et al. \(2002\)](#). For more

information about the implementation of the single star evolution in COMPAS see the corresponding section in the upcoming methods paper (Team COMPAS: J. Riley et al. (in prep)).

Mass Transfer: In determining the stability of mass transfer we use the ζ -prescription, which compares the radial response of the star with the response of the Roche lobe radius to the mass transfer (e.g. [Hjellming & Webbink 1987](#)). The mass transfer efficiency, $\beta = \Delta M_{\text{acc}}/\Delta M_{\text{don}}$, is defined as the fraction of the mass transferred by the donor that is actually accreted by the accretor. We limit the maximum accretion rate for stars to $\Delta M_{\text{acc}}/\Delta t \leq 10M_{\text{acc}}/\tau_{\text{KH}}$, where τ_{KH} is the Kelvin-Helmholtz timescale of the star ([Paczynski & Sienkiewicz 1972; Hurley et al. 2002](#)). The maximum accretion rate for double compact objects is limited to the Eddington accretion rate. If more mass than these rates is accreted then we assume that the excess is lost through isotropic re-emission in the vicinity of the accreting star, thus varying β (e.g. [Masseyvitch & Yungelson 1975; Soberman et al. 1997](#)). We assume that all mass transfer phases from a stripped post-helium-burning-star (case BB) onto a neutron star or black hole are unstable ([Tauris et al. 2015](#)).

Common Envelope: A common envelope phase follows dynamically unstable mass transfer and we parameterise this using the α - λ prescription from [Webbink \(1984\)](#) and [de Kool \(1990\)](#). We assume $\alpha = 1$, such that all of the gravitational binding energy is available for the ejection of the envelope. For λ we use the fitting formulae from [Xu & Li \(2010a,b\)](#). We assume that any Hertzsprung gap donor stars that initiate a common envelope phase will not survive this phase due to a lack of a steep density gradient between the core and envelope ([Taam & Sandquist 2000; Ivanova & Taam 2004](#)). This follows the ‘pessimistic’ common envelope scenario (c.f. [Belczynski et al. 2007](#)). We remove any binaries where the secondary immediately fills its Roche lobe upon the conclusion of the common envelope phase as we treat these as failed common envelope ejections.

Supernovae: We draw the remnant masses and natal kick magnitudes from different distributions depending on the type of supernova that occurs. For stars undergoing a general core-collapse supernova, we use the *delayed* supernova remnant mass prescription from [Fryer et al. \(2012\)](#). The *delayed* prescription does not reproduce the neutron star black hole mass gap and we use this as our default as it has been shown to provide a better fit for observed populations of DCOs (e.g. [Vigna-Gómez et al. 2018](#)). We draw the natal kick magnitudes from a Maxwellian velocity distribution with a one-dimensional root-mean-square velocity dispersion of

$\sigma_{\text{rms}}^{\text{1D}} = 265 \text{ km s}^{-1}$ (Lyne & Lorimer 1994; Hobbs et al. 2005).

We assume that stars with helium core masses between $1.6\text{--}2.25 M_{\odot}$ (Hurley et al. 2002) experience electron-capture supernovae (ECSN) (Nomoto 1984, 1987; Ivanova et al. 2008). We set all remnant masses to $1.26 M_{\odot}$ in this case as an approximation of the solution to Equation 8 of Timmes et al. (1996). For these supernovae, we set $\sigma_{\text{rms}}^{\text{1D}} = 30 \text{ km s}^{-1}$ (e.g. Pfahl et al. 2002; Podsiadlowski et al. 2004).

We assume that stars that undergo case BB mass transfer (Dewi et al. 2002) experience extreme stripping which leads to an ultra-stripped supernova (Tauris et al. 2013, 2015). For these supernovae we calculate the remnant mass using the Fryer et al. (2012) prescription and use $\sigma_{\text{rms}}^{\text{1D}} = 30 \text{ km s}^{-1}$ (as with ECSN).

Stars with final helium core masses between $60\text{--}135 M_{\odot}$ are presumed to undergo a pair-instability, or pulsational pair-instability supernova (e.g. Woosley et al. 2007; Farmer et al. 2019). We follow the prescription from Marchant et al. (2019) as implemented in (Stevenson et al. 2019) for these supernovae.

We assume that kicks are isotropic in the frame of the collapsing star. We adopt a maximum neutron star mass of $2.5 M_{\odot}$ (e.g. Kalogera & Baym 1996; Fryer et al. 2015; Margalit & Metzger 2017) for the fiducial model and change the Fryer et al. (2012) prescription accordingly.

Wind mass loss: We follow the wind prescription from Belczynski et al. (2008), which was based on results from Monte Carlo radiative transfer simulation of Vink et al. (2000, 2001). We use the wind mass loss rates from Vink et al. (2001) for stars above 12500 K and the rates from Hurley et al. (2000) for cooler stars. Additionally, we use a separate, higher wind mass loss rate for LBV stars, since these experience eruptive mass loss in addition to the regular line-driven winds and we follow Belczynski et al. (2008) in setting $f_{\text{LBV}} = 1.5$. We also use their Wolf-Rayet-like mass loss rate for helium stars and set $f_{\text{WR}} = 1$. See Team COMPAS: J. Riley et al. (in prep), Section 3 for the explicit equations.

2.1.3. Model variations

In addition to our fiducial model for the formation of DCOs, we explore 19 other models in which we change various aspects of the mass transfer, common envelope, supernova and wind mass loss physics assumptions in order to assess the effect of their uncertainties on the overall double compact object detection rates and distributions. Each of the models varies a single physics assumption (fiducial assumptions are outlined in Section 2.1.2) and these are outlined in Table 1.

Our fiducial model is labelled model A. Models B-F focus on changes to the mass transfer physics assumptions. We explore the effect of fixing the mass transfer efficiency β to a constant value, rather than allowing it to vary based on the maximum accretion rate. In models B, C, D, in which we set the value of β to 0.25, 0.5 and 0.75 respectively. In model E we investigate the consequence of assuming that case BB mass transfer onto a neutron star or black hole is always stable rather than always unstable.

Models G-K focus on altering the common envelope physics. We change the common envelope efficiency parameter to $\alpha_{\text{CE}} = 0.1, 0.5, 2.0, 10.0$ in models G, H, I and J respectively. In model K, we relax our restriction that Hertzsprung gap donor stars cannot survive common envelope events, thereby following the ‘optimistic’ common envelope scenario. We combine this with model E in model F.

In models L-R we consider changes related to our assumptions about supernova physics. Model L uses the alternate *rapid* remnant mass prescription from Fryer et al. (2012) instead of the *delayed* prescription. We change the maximum neutron star mass in models M and N to 2 and $3 M_{\odot}$ respectively to account for the range of predicted maximum neutron star masses. Model O removes the implementation of pair-instability and pulsational pair-instability supernovae. In models P and Q we decrease the root-mean-square velocity dispersion for core-collapse supernovae to explore the effect of lower kicks. Lastly, model R removes the natal kick for all black holes.

Finally, in models S-T we investigate the effect of changing our assumption about wind mass loss rates, specifically for Wolf-Rayet winds. We vary f_{WR} to 0.1 and 5.0 in models S and T respectively. These values approximately span the current range of possible Wolf-Rayet wind efficiencies suggested from observations (e.g. Vink (2017), Hamann et al. (2019), Shenar et al. (2019), Miller-Jones et al. (2021) and van Son et al. (in prep)).

2.2. Galaxy synthesis

In order to estimate a detection rate of DCOs with statistical uncertainties, we create a series of random instances of the Milky Way, each populated with a subsample drawn (with replacement) from the synthesised binaries described in Section 2.1.

Most previous studies that predict a detection rate for LISA place binaries in the Milky Way independently of their age or evolution. We improve upon this as the first study to use an empirically-informed analytical model of the Milky Way that takes into account the galaxy’s enrichment history by applying the metallicity-radius-

Model	Physics Variation
A	Fiducial (see Section 2.1.2)
B	Fixed mass transfer efficiency of $\beta = 0.25$
C	Fixed mass transfer efficiency of $\beta = 0.5$
D	Fixed mass transfer efficiency of $\beta = 0.75$
E	Case BB mass transfer is always unstable
F	Model E + Model K
G	CE efficiency parameter $\alpha = 0.1$
H	CE efficiency parameter $\alpha = 0.5$
I	CE efficiency parameter $\alpha = 2$
J	CE efficiency parameter $\alpha = 10$
K	HG donor stars initiating a CE survive CE
L	Fryer rapid SN remnant mass prescription
M	Maximum NS mass is fixed to $2 M_{\odot}$
N	Maximum NS mass is fixed to $3 M_{\odot}$
O	PISN and pulsational-PISN not implemented
P	$\sigma_{\text{rms}}^{\text{1D}} = 100 \text{ km s}^{-1}$ for core-collapse supernova
Q	$\sigma_{\text{rms}}^{\text{1D}} = 30 \text{ km s}^{-1}$ for core-collapse supernova
R	Black holes receive no natal kick
S	Wolf-Rayet wind factor $f_{\text{WR}} = 0.1$
T	Wolf-Rayet wind factor $f_{\text{WR}} = 5.0$

Table 1. A description of the 20 binary population synthesis models used in this study. A is the fiducial model, B-F change mass transfer physics, G-K change common envelope physics , L-R change supernova physics and S-T change wind mass loss (c.f. Broekgaarden et al. 2021, Table 2).

time relation from Frankel et al. (2018). The authors developed this relation in order to measure the global efficiency of radial migration in the Milky Way and calibrated it using a sample of red clump stars measured with APOGEE (Majewski et al. 2017).

In Section 2.2.1, we outline our model for the Milky Way and in Section 2.2.2 we explain how we combine our population of synthesised DCOs with this Milky Way model.

2.2.1. Milky Way model

Our model for the Milky Way accounts for the low- α ⁶ disc, high- α disc and central bar/bulge. The low- and high- α discs are often also referred to as the thin and thick discs. We use the α nomenclature as there is a clear bimodal distribution in the chemical plane, allowing stars to be easily decomposed into the two disc components, as opposed to the vertical distribution which cannot be fit by a single exponential but is not easy to

⁶Note that α in this case refers to the abundance of α process elements and is *not* related to the common envelope efficiency α_{CE} .

split into separate components. For each of the three components, we use a separate star formation history, radial and vertical distribution, which we combine into a single model, weighting each component by its stellar mass. Licquia & Newman (2015) gives that the stellar mass of the bulge is $0.9 \times 10^{10} M_{\odot}$ and the stellar mass of the disc is $5.2 \times 10^{10} M_{\odot}$, which we split equally between the low- and high- α discs (e.g., Snaith et al. 2014).

Star formation history: We use an exponentially declining star formation history (Frankel et al. 2018) (a priori inspired by average the cosmic star formation history) for the combined low- and high- α disks, where the two disks transition at about 8 Gyr ago, and re-normalize the produced mass to be equal in each of the two components.

$$p(\tau) \propto \exp\left(-\frac{(\tau_m - \tau)}{\tau_{\text{SFR}}}\right), \quad (2)$$

where τ is the lookback time (the amount of time elapsed between the binary's zero-age main sequence and today), $\tau_m = 12$ Gyr is the assumed age of the Milky Way and $\tau_{\text{SFR}} = 6.8$ Gyr is the star formation timescale.

The star formation history of the Milky Way bulge (which we assume here to be dominated by the central bar) has many uncertainties due to (1) sizeable age measurement uncertainties at large ages in observational studies, (2) complex selection processes affecting the observed age distributions, and (3) formation mechanisms still under debate. But the bulge was shown to contain stars with an age range of 6-12 Gyr (e.g., Bovy et al. 2019), where the younger tail of ages might come from the growth of the Galactic bar. To model the bulge age distribution more realistically than in previous studies (assuming an older bulge coming from a single starburst), we choose to adopt a star formation history using a $\beta(2, 3)$ distribution, shifted and scaled such that stars are only formed in the range [6, 12] Gyr

Radial distribution: For each of the three components we employ the same single exponential distribution (but with different scale lengths)

$$p(R) = \exp\left(-\frac{R}{R_d}\right) \frac{R}{R_d^2}, \quad (3)$$

where R is the Galactocentric radius and R_d is the scale length of the component. For the low- α disc, we set $R_d = R_{\text{exp}}(\tau)$, where $R_{\text{exp}}(\tau)$ is the scale length presented in Frankel et al. (2018, Eq. 5)

$$R_{\text{exp}}(\tau) = 4 \text{ kpc} \left(1 - \alpha_{R_{\text{exp}}} \left(\frac{\tau}{8 \text{ Gyr}}\right)\right), \quad (4)$$

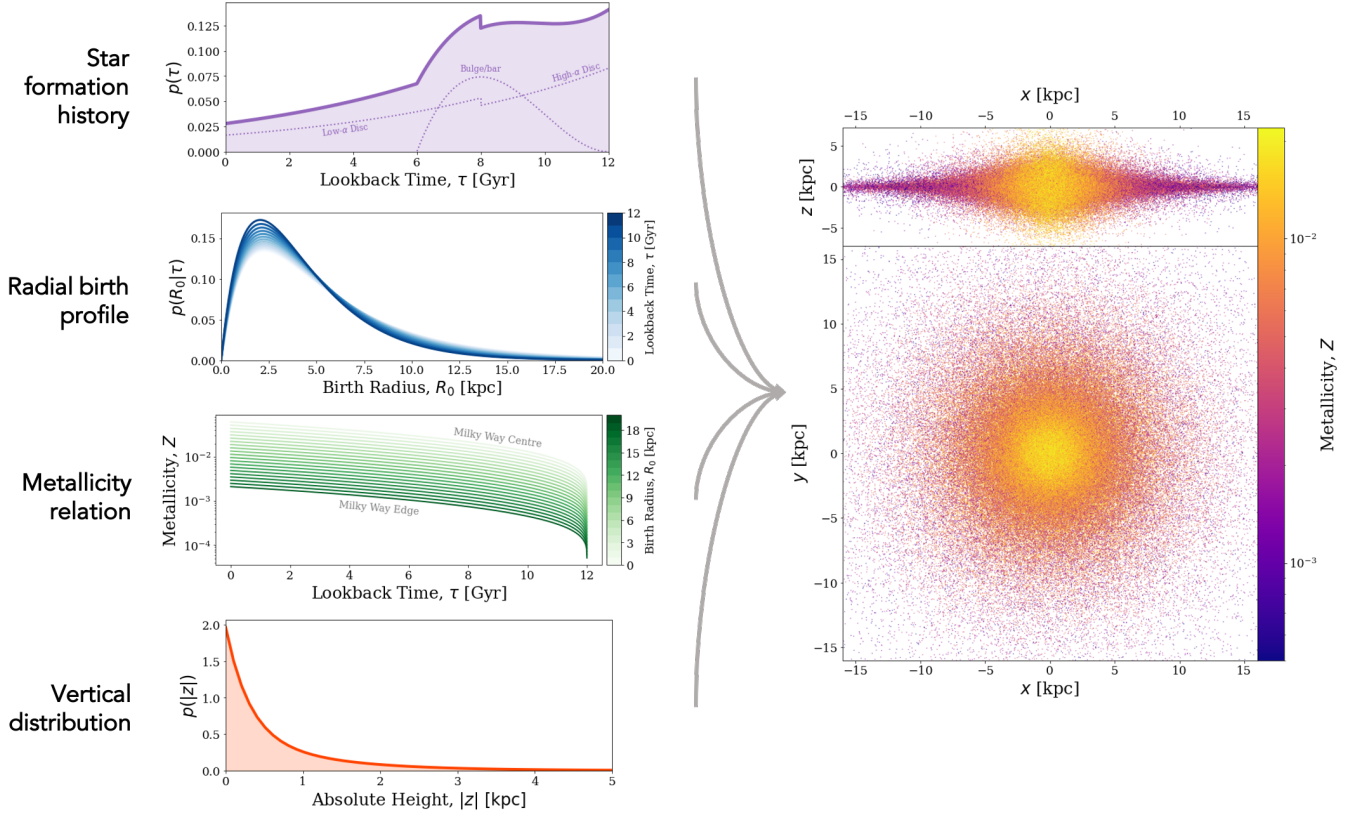


Figure 1. A schematic illustrating how we create a mock Milky Way galaxy. The left panel illustrates the different model aspects: star formation history of 3 galactic components (individually shown in the dotted lines), spatial distribution at birth, age-metallicity-radius relation, and vertical distribution. On the right, we show an example instance of the Milky Way with 250000 binaries shown as points colour coded by metallicity. The top panel shows a side-on view and the bottom panel shows a face-on view.

where $\alpha_{R_{\text{exp}}} = 0.3$ is the inside-out growth parameter⁷. This scale length accounts for the inside-out growth of the low- α disc and hence is age dependent. We assume $R_d = (1/0.43)$ kpc for the high- α disc (Bovy et al. 2016, Table 1) and $R_d = 1.5$ kpc for the bar component (Bovy et al. 2019).

Vertical distribution: Similar to the radial distribution, we use the same single exponential distribution (but with different scale heights) for each component

$$p(|z|) = \frac{1}{z_d} \exp\left(-\frac{|z|}{z_d}\right), \quad (5)$$

where z is the height above the Galactic plane and z_d is the scale height. We set $z_d = 0.3$ kpc for the low- α disc (McMillan 2011) and $z_d = 0.95$ kpc for the high- α disc (Bovy et al. 2016). [TODO: Neige to Tom: for bar, I will think more for your bar scale-height, but the exact value should not change your results much since

⁷In $R_{\text{exp}}(\tau)$, we use 4 kpc instead of 3 kpc for the 0 Gyr exponential scale-length of the disc as NF finds that it provides a better fit to the original data

they will only slightly change the distance distribution of your sources, but not the rates nor the normalization.] For the bulge, we set $z_d = 1.5$ kpc such that the probability of forming a star approaches zero at approximately the co-rotation radius of the Galactic bar/bulge (Bovy et al. 2019). [TODO: @Neige, did I justify the bulge/bar height correctly? A: The vertical distribution should not influence at which radius the bar should stop forming stars – more later]

Metallicity-radius-time relation: The relation is given by (Frankel et al. 2018, Eq. 7)

$$\begin{aligned} [\text{Fe}/\text{H}](R, \tau) &= F_m + \nabla[\text{Fe}/\text{H}]R \\ &- \left(F_m + \nabla[\text{Fe}/\text{H}]R_{[\text{Fe}/\text{H}=0]}^{\text{now}} \right) f(\tau), \end{aligned} \quad (6)$$

where

$$f(\tau) = \left(1 - \frac{\tau}{\tau_m}\right)^{\gamma_{[\text{Fe}/\text{H}]}} , \quad (7)$$

$F_m = -1$ dex is the metallicity of the gas at the center of the disc at $\tau = \tau_m$, $\nabla[\text{Fe}/\text{H}] = -0.075 \text{ kpc}^{-1}$ is the metallicity gradient, $R_{[\text{Fe}/\text{H}=0]}^{\text{now}} = 8.7$ kpc is the radius at which the present day metallicity is solar and $\gamma_{[\text{Fe}/\text{H}]} =$

0.3 set the time dependence of the chemical enrichment. We can convert this to the representation of metallicity that we use in this paper by applying (e.g Bertelli et al. 1994)

$$\log_{10}(Z) = 0.977[\text{Fe}/\text{H}] + \log_{10}(Z_\odot). \quad (8)$$

Although Frankel et al. (2018) only fit this model for the low- α disc, we also use this metallicity-radius-time relation for the high- α disk and the bar, but focusing on the chemical tracks more representative to the inner disk and large ages. Sharma et al. (2020) showed that using a simple continuous model for both the low- and high- α discs, the Milky Way abundance distributions could be well reproduced. Empirically, the chemical tracks in the $[\alpha/\text{Fe}]\text{-}[\text{Fe}/\text{H}]$ plane of the stars in the bulge/bar follow the same track as those of the old stars in the Solar neighbourhood (Bovy et al. 2019, Fig. 7), which motivates our modelling choice to use the same metallicity-radius-time relation.

Fig. 1 shows the distributions and relations outlined in this section and also displays an example random galaxy drawn using this model.

2.2.2. Combining population and galaxy synthesis

For each Milky Way instance, we randomly sample the following set of parameters

$$\mathbf{g}_i = \{\tau, R, Z, z, \theta\} \quad (9)$$

for $i = 1, 2, \dots, N_{\text{MW}}$, where we set $N_{\text{MW}} = 2 \times 10^5$, τ, R, Z and z are defined and sampled using the distribution functions specified in Section 2.2.1, θ is the polar angle sampled uniformly on $[0, 2\pi]$ and Z is the metallicity. Figure 1 shows an example of a random Milky Way instance created with these distributions. This shows how these distributions translate to positions in the Milky and illustrates the gradient in metallicity over radius.

We match each set of galaxy parameters \mathbf{g}_i , to a random set of binary parameters $\mathbf{b}_{Z,i}$, by randomly drawing a set of binary parameters from the closest metallicity bin to the metallicity in \mathbf{g}_i .

Each binary is likely to move from its birth orbit. Although all stars in the Galactic disc experience radial migration (Sellwood & Binney 2002; Frankel et al. 2018), double compact objects generally experience stronger dynamical evolution as a result of the effects of both Blaauw kicks (Blaauw 1961) and natal kicks (e.g. Hobbs et al. 2005).

The magnitude of the systemic kicks are typically small compared to the initial circular velocity of a binary at each Galactocentric radius. Therefore, kicks will

not significantly alter the overall distribution of their positions. Given this, and for the sake of computational efficiency, we do not account for the displacement due to systemic kicks in our analysis.

2.3. Gravitational wave detection

We use the Python package **LEGWORK** to evolve binaries and calculate their LISA detectability. For a full derivation of the equations given below please see the **LEGWORK** release paper (Wagg et al. in prep) or documentation.

2.3.1. Inspiral evolution

Each binary loses orbital energy to gravitational waves throughout its lifetime. This causes the binary to shrink and circularise over time. In order to assess the detectability of a binary, we need to know its eccentricity and frequency at the time of the LISA mission. For each binary in our simulated Milky Way, we know that the time from DCO formation to today is $\tau - t_{\text{evolve}}$ and that the initial eccentricity and semi-major axis are e_{DCO} and a_{DCO} . We find the eccentricity of the binary at the start of the LISA mission, e_{LISA} , by numerically integrating its time derivative (Peters 1964, Eq. 5.13) given the initial conditions. This additionally can be converted to the semi-major axis at the start of LISA, a_{LISA} (Peters 1964, Eq. 5.11), which in turn gives the orbital frequency, $f_{\text{orb},\text{LISA}}$, by Kepler's third law.

2.3.2. Binary detectability

We define a binary as detectable if its gravitational wave signal has a signal-to-noise ratio of greater than 7 (e.g. Breivik et al. 2020; Korol et al. 2020). The sky-, polarisation- and orientation-averaged signal-to-noise ratio, ρ , of an inspiraling binary can be calculated with the following (e.g. Finn & Thorne 2000)

$$\rho^2 = \sum_{n=1}^{\infty} \int_{f_{n,i}}^{f_{n,f}} \frac{h_{c,n}^2}{f_n^2 S_n(f_n)} df_n, \quad (10)$$

where n is a harmonic of the gravitational wave signal, $f_n = n \cdot f_{\text{orb}}$ is the frequency of the n^{th} harmonic of the gravitational wave signal, f_{orb} is the orbital frequency, $S_n(f_n)$ is the LISA sensitivity curve at frequency f_n (e.g. Robson et al. 2019) and $h_{c,n}$ is the characteristic strain of the n^{th} harmonic, given by (e.g. Barack & Cutler 2004)

$$h_{c,n}^2 = \frac{2^{5/3}}{3\pi^{4/3}} \frac{(G\mathcal{M}_c)^{5/3}}{c^3 D_L^2} \frac{1}{f_{\text{orb}}^{1/3}} \frac{g(n,e)}{nF(e)}, \quad (11)$$

where D_L is the luminosity distance to the source, f_{orb} is the orbital frequency, $g(n,e)$ and $F(e)$ are given in

Peters & Mathews (1963) and \mathcal{M}_c is the chirp mass, defined as

$$\mathcal{M}_c = \frac{(m_1 m_2)^{3/5}}{(m_1 + m_2)^{1/5}}. \quad (12)$$

We use LEGWORK to calculate the signal-to-noise ratio for each binary and the package ensures that enough harmonics are computed for each binary such that the error on the gravitational wave luminosity remains below 1%.

2.3.3. Detection rate calculation

For each physics variation model and DCO type, we compute the total number of merging DCOs in the Milky Way today, N_{MW} , based on the COMPAS simulation. This takes into account the true mass and IMF of the Milky Way since our simulations may each have a slightly different galaxy mass and only ever sample from massive stars rather than the full IMF. For a more in-depth discussion of this process see Appendix A.

We determine the fraction of binaries that are detectable in each Milky Way instance by summing the adaptive importance sampling weights of the binaries that have an SNR greater than 7 and dividing by the total weights in the simulation. We multiply this fraction by the total number in the Milky Way to find a detection rate.

$$N_{\text{detect}} = \frac{\sum_{i=0}^{N_{\text{detect}}} w_i}{\sum_{i=0}^{N_{\text{DCO}}} w_i} \cdot N_{\text{MW}} \quad (13)$$

We calculate the detection rate by Monte Carlo sampling 2500 Milky Way instances (each containing 200,000 DCOs) for each DCO type and every physics variation in order to obtain values for the uncertainty on the expected detection rate.

3. RESULTS

In this section we present our main results for the detectable LISA DCO population. We find that, for our fiducial model, a four year LISA mission will detect $30.6^{+51.1}_{-20.5}$ BHBHs, $26.4^{+48.5}_{-17.3}$ BHNSs and $7.1^{+10.8}_{-4.8}$ NSNSs where the error bars represent the 90% confidence interval. We first show the distribution of the sources on the sensitivity curve in Section 3.1, before exploring the variations in the detection rate over different physics variations in Section 3.2 and analysing the parameter distributions for detectable sources in the fiducial model in Section 3.3.

3.1. Distribution on the sensitivity curve

We illustrate the distribution of detectable DCOs on the LISA sensitivity curve in Figure 2. This shows that

the detectable population of these massive DCOs is concentrated at comparatively lower frequencies than the LISA verification binaries (shown as stars in the top panel) and the more numerous WDWD population (e.g. Korol et al. 2017). This is expected since producing the same SNR as a BHBH, BHNS or NSNS with a relatively lower mass (circular) WDWD requires a higher frequency. This finding is in agreement with Sesana et al. (2020) and as noted in that work, this could possibly be used to distinguish these more massive DCOs from WDWDs. There are several other notable features in these distributions and we plot grid lines of constant distance and inspiral time to help to explain the shape of the distribution.

The straight diagonal lines show where a binary at a fixed distance and with the average chirp mass (annotated in each panel) would lie on the sensitivity curve for different frequencies. We would therefore expect that if a population was entirely circular, it should be bounded approximately between the 0.1–30 kpc lines (roughly the minimum and maximum distance to a source in the Milky Way). From inspection of the bottom panels with each individual DCO type we see that, though this is the true for a large fraction of the population, there is a distinct subpopulation of binaries that extend downwards, especially around 2 mHz. This offshoot is composed of eccentric binaries for which the circular distance contours do not apply. For instance, we plot the 90% contour of only the circular sources in our sample over the density distribution in each of the bottom panels and it is clear that the circular subsample is bounded by the distance lines. We also plot a line of constant distance at 30 kpc for an eccentric binary with $e = 0.98$ to show the differences for eccentric sources. Additionally, we note that the peak of the density distribution coincides with the centre of the Milky Way as expected, since binaries are most likely to be formed towards the centre of the Galaxy.

We plot vertical lines that give the inspiral time for a circular binary with the average chirp mass (annotated in each panel). From these lines we can understand the trend of the density distribution decreasing with increasing frequency. Sources with higher frequencies have shorter inspiral times and thus DCOs will spend less time in these regimes, meaning that more sources are detected at lower frequencies. Note that these inspiral time lines should only be used as guidelines for the population as a whole, as the inspiral time of each individual source will be a function of its mass and eccentricity. It is also evident for each DCO source that the tail of the high frequency sources is more numerous near to the Galactic centre than at short distances. This



Figure 2. Density distribution of detectable DCOs plotted over the LISA sensitivity curve, where each panel corresponds to **top:** combined density plot for all DCO types (BHBH, BHNS and NSNS) **bottom:** three panels with individual density distribution of different DCO types. In each panel, we plot the total signal of binaries at their dominant frequency $n f_{\text{orb}}$, such that n is the harmonic that produces the most relative gravitational wave luminosity ($n = 2$ for circular binaries). If the density of points is below our lowest contour (2%) then we plot the points as scatter points, where their sizes corresponds to their STROOPWAFEL weights. The inset colourbars indicate the percentage of the population represented by each contour and the annotated mass is the average chirp mass for all binaries in the panel, which is used in plotting the grid lines. We plot diagonal lines of constant distance, where the straight lines show the signal for a circular binary of average chirp mass, whilst the curved line shows the signal for an eccentric binary with $e = 0.98$. The vertical lines indicate the inspiral time for a circular binary with the average chirp mass. In the top panel we overlay the LISA verification binaries from Kupfer et al. (2018). In the bottom panels we add the 90% contour line for only the circular sources to show how the distribution changes without eccentric sources present.

is simply because there are more sources in the galactic centre and so the chances of ‘catching’ a binary at high frequency are better.

3.2. Detection rates

[TODO: I will be updating this section once the other physics variations are done running. There will be a couple of new models and the current ones will have better high Z resolution.] We find that for our fiducial model, a four year LISA mission will detect $30.6^{+51.1}_{-20.5}$ BHBHs, $26.4^{+48.5}_{-17.3}$ BHNSs and $7.1^{+10.8}_{-4.8}$ NSNSs, where the error bars represent the 90% confidence interval. Increasing the LISA mission length to ten years changes the number of detections to $50.6^{+63.3}_{-29.2}$, $46.2^{+99.3}_{-25.7}$ and $12.1^{+13.5}_{-6.9}$ respectively. In Figure 3, we show the expected number of LISA detections for each model variation and discuss the prominent trends in the following sections. We show the rates and uncertainties plotted in this figure in Table 2.

3.2.1. BHBH detection rate trends

The BHBH detection rate is markedly robust across physics variations, with the expected detections in each model staying within 25% of the fiducial rate (with the exception of model K). Thus even if there are changes in our understanding of the underlying physics before the LISA mission commences, the expected BHBH detection rate is unlikely to change significantly.

The exception to this statement is model K, in which we allow Hertzsprung gap donors to survive common envelope events. A large fraction of the progenitors of BHs in this mass range expand significantly during the Hertzsprung gap phase and initiate common envelope events. Therefore, though the detectable fraction does not change significantly, the increased population of BHBHs in the Milky Way leads to this model predicting 2.5 times more detections.

3.2.2. BHNS detection rate trends

In contrast, the BHNS detection rate is very sensitive to changes in binary physics assumptions. Therefore, once LISA flies and we know the actual number of detections, we can compare to each model and possibly provide some constraint on binary evolution physics. There are several notable trends in the BHNS detection rate in the middle pane of Figure 3.

As β increases in models B-D, the BHNS detection rate steadily decreases. This may seem unintuitive since a higher mass transfer efficiency should lead to more massive compact objects and thus a more detectable population. However, one must also consider that most of these DCOs are formed through a common envelope event and so retaining more of the envelope during mass transfer means that the eventual ejection of the envelope

is much more difficult, thus leading to more stellar mergers and fewer detectable BHNSs (e.g. Kruckow et al. 2018).

[TODO: @ALL, the trend with common envelopes still confuses me, specifically, why does it not increase when $\alpha = 2.0$? We never quite resolved this in the thread in zpro_tom_wagg with me and Lieke. I do see that the BHBH have a lot of only stable mass transfer and so reasonably are not too affected. NSNS basically only come through CE events and so sensibly are strongly affected but BHNS have $\sim 70\%$ classic channel and so should be affected strongly. But we don’t see an increase with $\alpha = 2.0$. Any thoughts? (I’m leaving thinking about this for now in case it changes with the new data haha)]

Enforcing that case BB mass transfer is always unstable (model E) decreases the detection rate as fewer NSs are produced and thus fewer BHNSs form. This is explained in further detail in Section 3.2.3. For the same reason as the BHBH rate, model K has a higher number of detections. This change is less prominent than in the BHBH case as the progenitors tend to be lower masses and initiate a CE event less frequently during the Hertzsprung gap phase.

The Fryer *rapid* prescription (model L) leads to a higher detection rate for BHNSs because progenitors that would become black holes in the *delayed* prescription, instead become neutron stars and so more BHNSs are formed instead of BHBHs. For the same reason, increasing the maximum neutron star mass (model N) increases the detection rate and the inverse is true when it is decreased (model M).

Finally, models P-R show increased detection rates since lower kicks result in fewer disrupted binaries and hence a more numerous detectable population. Following this logic it makes sense that model Q produces more detections than model P. The model with no BH kick (R) is slightly lower than model Q as the number of surviving binaries is limited by the neutron star kick more than the black hole kick.

3.2.3. NSNS detection rate trends

As β increases the NSNS detection rate increases, the opposite trend to that seen in the BHNS rate. This is for two main reasons: firstly the ejection of a common envelope is less problematic for the less massive NSNS binaries. Moreover, the increased mass transfer efficiency means that systems that were previously below the mass necessary to become a NS can now accrete enough mass to form a NS. Although the same is true for more massive stars becoming BHs instead of NSs, due

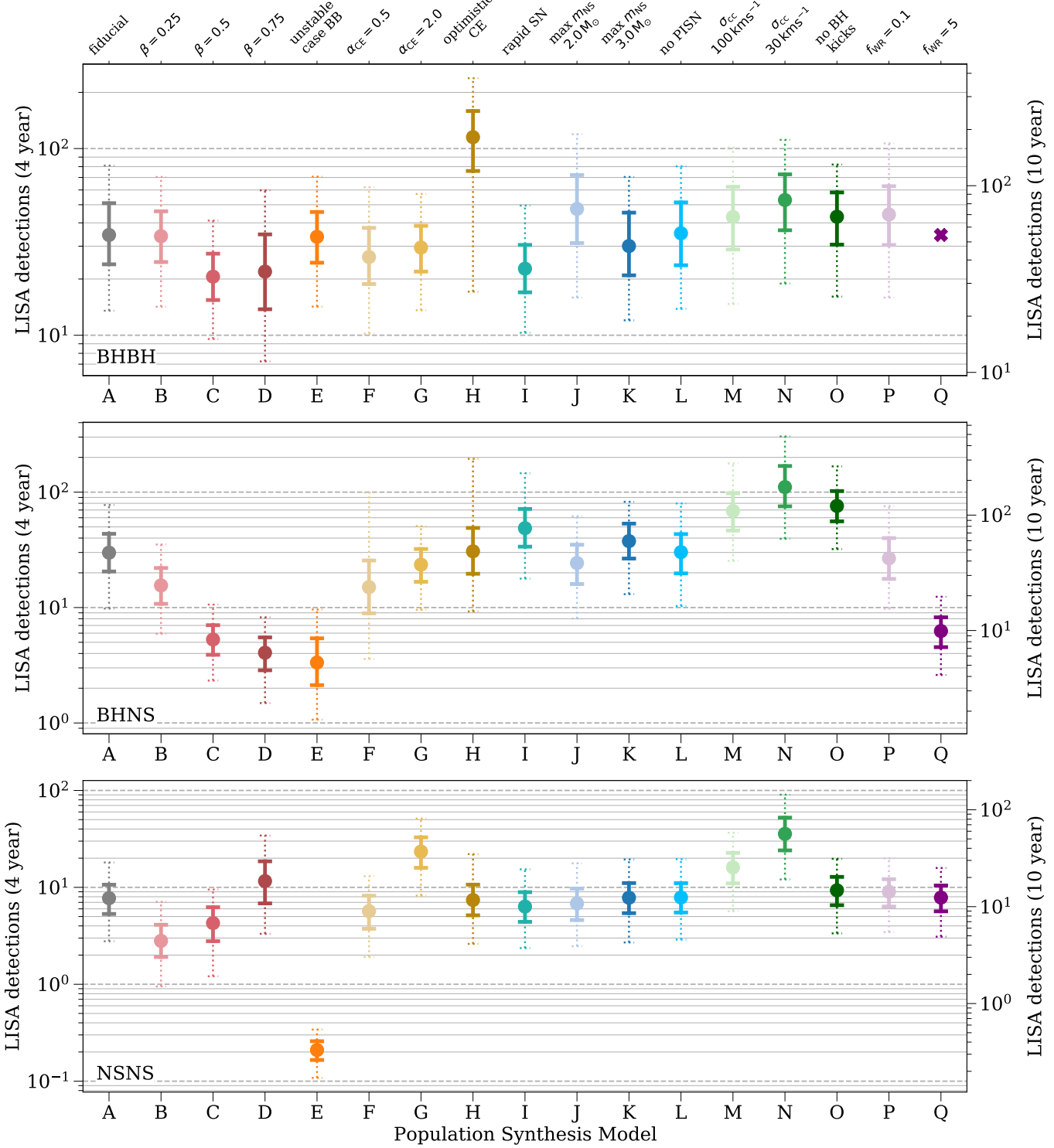


Figure 3. The number of expected detections in the LISA mission for different DCO types and model variations. Error bars show the 50% (solid) and 90% (dotted) confidence intervals. The left axis and grid lines show the number of detections in a four year LISA mission and the right axis shows an approximation of the number of detections in a 10 year mission (we scale the axis by $\sqrt{T_{\text{obs}}}$, see Table 2 for exact rates). Each model is described in further detail in Table 1 and details of the fiducial assumptions are in Section 2.1.2. [TODO: subject to change with the updated/new models]

to the IMF, there is a net flux of more stars becoming NSs.

There is a drastic decrease in detections for model E by nearly two orders of magnitude. This is because the majority of NSNS binaries are formed through case BB mass transfer and setting this mass transfer to be always unstable results in many of these binaries to merge before they could become NSNSs. As a result the total number of detections decreases, however, interestingly the remaining population represent more massive progenitors (that would not go through case BB mass transfer) and thus is skewed to higher masses and has a *higher* detectable fraction.

The vast majority of NSNSs in our sample are formed through the common envelope channel and thus changing the value of α_{CE} has an effect on the rate. We see that decreasing α_{CE} (model H) leads to a lower rate as there is less energy available to eject the envelope and so more binaries result to stellar mergers rather than NSNSs and similarly we see an inverse trend when increasing α_{CE} (model I).

As we found in the BHNS trends, a lower value for the core-collapse supernova velocity dispersion increases the detection rate in models P and Q, whilst changing the PISN or BH kick prescription (models O and R) of course has no effect on the NSNS population.

3.3. Distributions for the fiducial model

In Figure 4, we show the distribution of the individual parameters of the population of detectable binaries and discuss the various features in the following sections.

3.3.1. Black Hole Mass

For both the BHBHs and BHNSs, the black hole mass distribution extends across relatively low masses, with 88% and 90% respectively below $11 M_\odot$. This is because, at the high metallicities in the Milky Way, stellar winds are much stronger and strip away much of the stellar mass before BH formation. The mass distribution extends down to $2.5 M_\odot$, our fiducial maximum neutron star mass, since the Fryer et al. (2012) *delayed* remnant mass prescription does not produce a mass gap between neutron stars and black holes. Indeed we expect 35% and 39% of detected BHBH and BHNS systems to contain a black hole in the lower mass gap. Therefore, LISA could help to confirm or rule out the existence of the lower mass gap.

The bimodality of the BHBH distribution is a result of most detectable BHBHs in our sample having unequal mass ratios. The two peaks are from the primary and secondary black hole masses, which peak around $8 M_\odot$ and $3.5 M_\odot$ respectively. We show these individ-

ual distributions as dotted curves below the main BHBH distribution.

The reasoning for these unequal mass ratio systems is as follows: in order to produce a BHBH, most formation channels require at least the first mass transfer to be stable. This stability is strongly dependent on the mass ratio such that equal mass ratios (at the moment of mass transfer) are preferred for creating BHBHs. Yet, since stellar winds are so strong at high metallicity, and even stronger for more massive stars, the primary star will experience significant mass loss and so an initially *unequal* mass ratio is preferred so that the masses are more balanced at the first instance of mass transfer. Since mass transfer occurs after the end of the main sequence for most of our BHBHs, the star will have a well defined core and these core masses, which go on to form BHs, will reflect the initially unequal mass ratios.

3.3.2. Neutron Star Mass

The neutron star mass distribution shows that most neutron stars have low masses, with 77% and 91% having masses below $1.7 M_\odot$ for BHNSs and NSNSs respectively. The lack of neutron stars around $1.7 M_\odot$ and the subsequent small peaks are artifacts of the discontinuous nature of the Fryer et al. (2012) remnant mass prescription and do not have strong effects since the vast majority of NSs are formed with lower masses.

Both distributions have notable peaks around $1.26 M_\odot$, though more strongly in the NSNS case, which are a result of the combination of two effects. Firstly, we set the remnant mass for all electron-capture supernovae to $1.26 M_\odot$ (see Sec. 2.1.2) and thus this leads to a pileup when many systems are formed through ECSN. In addition, the Fryer remnant mass prescription gives a fixed fallback mass for any star with a CO core mass less than $2.5 M_\odot$, such that many NSs are given the identical mass of $1.278 M_\odot$ in the *delayed* prescription (see Fryer et al. 2012, Eq. 19).

3.3.3. Orbital Frequency

The orbital frequency distributions for BHBHs, BHNSs and NSNSs peak at progressively increasing frequencies. This is because a higher mass DCO at the same distance and eccentricity requires a lower frequency to produce the same signal-to-noise ratio and thus be detected. The BHBH distribution has a tail that extends to 8×10^{-6} Hz, which is comprised of highly eccentric binaries. These systems are still detectable by LISA as the high eccentricity means that the majority of the GW signal is emitted at higher harmonics at higher frequencies that are located in the LISA band. Similar tails are not as prevalent for BHNSs and NSNSs as they do not have as many eccentric binaries.

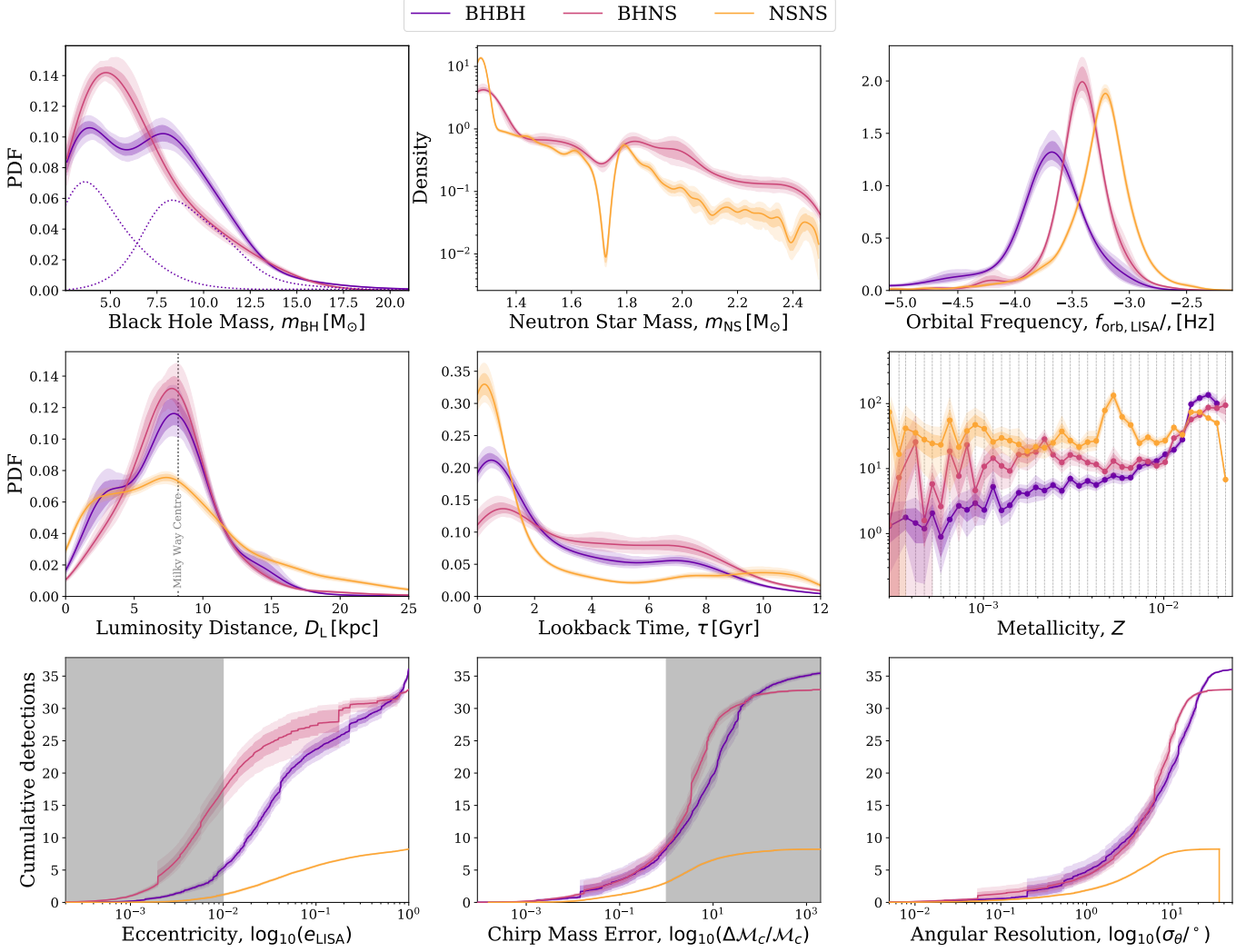


Figure 4. Distributions for various parameters of the DCOs that are detectable in a 4 year LISA mission in our fiducial model. Each panel shows the distribution of a single parameter, where the colour denotes the DCO type. We also plot the 1- and 2- σ uncertainties (obtained via bootstrapping) with the dark and light shaded areas respectively. The first two rows (excluding metallicity) use kernel density estimators to show the distributions. The dotted lines in the black hole mass panel show the individual distributions of the primary and secondary masses. The metallicity panel shows the distribution over the metallicity bins used in our population synthesis, which we show in the grid lines. The final three panels for the cumulative distribution functions for observables, normalised to the expected number of fiducial detections in a four year LISA mission. The dark shaded areas indicate regimes in which the quantity cannot be measured. The dotted lines in the angular resolution plot show the maximum angular resolution that can be covered by a single pointing of the labelled instrument. In Section 3.3 we discuss the features of the distributions.

3.3.4. Luminosity Distance

Each DCO's luminosity distance distribution peaks around 8 kpc since this is the distance to the centre of the Milky Way and thus the most dense location of DCOs. There is a clear bias in each distribution for systems at lower distances since closer binaries are easier to detect. This bias is most prominent for the NSNS distribution since, on average, their lower relative masses require a smaller distance in order to be detected.

3.3.5. Lookback Time

Although when creating each mock Milky Way galaxy the lookback time is drawn independently from other parameters, and in the same way for every DCO type, the distributions are clearly different for each type of DCO. This is because for a binary to be detectable, it must have an orbital frequency within the LISA band. Therefore a binary needs to have completed most of its inspiral to be visible in the LISA band and thus detectable systems will tend to have lookback time that are close to their merger times, which are a function of other binary parameters.

Since most of the DCOs are formed through common envelope events, their initial separations are relatively tight and so if a binary it given a long lookback time, it will have merged before the LISA mission. This explains the peak in each distribution at short lookback times. The later lookback times correspond to systems that are formed through channels in which mass transfer is only stable and no common envelope event occurs.

The trends across the different DCO types can be explained by considering that the merger time is a function of the masses, frequency and eccentricity of the source. This dependence can be approximately written as $t_{\text{merge}} \propto f_{\text{orb}}^{-4} m_1^{-3} (1-e^2)^{-7/2}$, (Peters 1964, Eq. 5.14). Therefore, although NSNSs are the lowest mass systems, their relatively higher orbital frequencies means that they have the shortest merger times. This same logic implies that BHNSs should have the next shortest merger times and then BHBHs. This order is flipped due to the fact that high eccentricity results in a shorter merger time and we find that LISA detectable BHNSs are mostly circular, whilst BHBHs have a significant highly eccentric subpopulation.

3.3.6. Metallicity

[TODO: Returning to this once I've made the plot that compares the Milky Way distribution and formation rates]

3.3.7. Eccentricity

The eccentricity distributions show that detectable BHBHs are the most eccentric of the three DCOs. This may seem counter-intuitive since neutron stars receive stronger natal kicks, which cause the orbit to become eccentric. However, these stronger kicks often instead result in disrupted or too-wide binaries in more weakly bound NSNSs. In contrast, BHBHs can receive strong kicks that impart high eccentricity without disrupting and thus tend to be more eccentric. This effect is compounded by the fact that we can see BHBHs at lower orbital frequencies, meaning that they have not had as much time to circularise and so still have significant eccentricity by the time of the LISA mission.

A significant fraction of DCOs in each population have eccentricities greater than 0.01, the lower bound on the measurable eccentricity with LISA proposed by Nishizawa et al. (2016), which we indicate with the shaded area. We discuss the estimation of the eccentricity uncertainty further in Section 3.4

3.4. Measurement Uncertainties

Although it is useful to investigate the underlying parameters of the detectable population, it is also impor-

tant to consider what LISA will actually *measure* during a detection.

3.4.1. Eccentricity uncertainty

One of the main advantage of space-based gravitational wave detectors such as LISA is that systems may still have significant eccentricity during the LISA mission. Whilst also being useful a useful individual quantity for learning more about sources, the uncertainty on the eccentricity also affects the uncertainty on the chirp mass and so it is important to quantify this uncertainty.

We follow a method used in previous works that uses the individually detectable harmonics of sources to determine the uncertainty of the eccentricity of a source (e.g. Lau et al. 2020; Korol & Safarzadeh 2021). Eccentric sources emit at several evenly spaced harmonic frequencies, each with a different fraction of the gravitational wave power and the distribution of the power over the harmonics changes with eccentricity. Therefore, by measuring the SNR of each individual harmonic and finding the ratio of the SNR of the two most detectable harmonics that are above the detection threshold, one can determine the eccentricity. The uncertainty on the eccentricity can therefore be written as a combination of the uncertainty on the SNR of the two most detectable harmonics. In the limit of large SNRs, the eccentricity uncertainty, Δe , can be written as

$$\Delta e = \frac{1}{\rho_1} + \frac{1}{\rho_2}, \quad (14)$$

where ρ_1 and ρ_2 are the SNRs of the two most detectable harmonics.

In some cases, sources may only have one individually detectable harmonics, or even none. In these cases one can only put a lower or upper bound on the eccentricity. For sources with only one detectable harmonic, the source is either a circular source or a source with a small enough eccentricity that most of the GW power is still concentrated in the $n = 2$. Therefore, we can use this information to place an upper bound on the eccentricity. Conversely, sources with no detectable harmonics must be eccentric such that the GW power has spread over so many harmonics that no single harmonic has a significantly stronger signal. Therefore, we can use this information to place a lower bound on the eccentricity.

This method provides a pessimistic estimate of the eccentricity of sources since we do not consider the benefits of any sort of matched-filter analysis or similar methods. We discuss how the pessimism of this method affects our results and some possible alternative in Section 4.3.

3.4.2. Chirp mass uncertainty

The chirp mass uncertainty can be calculated using the uncertainty on the orbital frequency, the time derivative of the orbital frequency and the eccentricity. This is because the time derivative of the orbital frequency can be written as

$$\dot{f}_{\text{orb}} = \frac{48}{5\pi} \frac{(G\mathcal{M}_c)^{5/3}}{c^3} (2\pi f_{\text{orb}})^{11/3} F(e), \quad (15)$$

where f_{orb} is the orbital frequency, \mathcal{M}_c is the chirp mass (defined in Eq. 12) and e is the eccentricity and

$$F(e) = \frac{1 + \frac{73}{24}e^2 + \frac{37}{96}e^4}{(1 - e^2)^{7/2}}, \quad (16)$$

is the enhancement factor of gravitational wave emission for an eccentric binary over an otherwise identical circular binary (Peters & Mathews 1963, Eq. 17).

We can invert this and instead write that the chirp mass is

$$\mathcal{M}_c = \frac{c^3}{G} \left(\frac{5\pi}{48} \frac{\dot{f}_{\text{orb}}}{F(e)} \right)^{3/5} \frac{1}{(2\pi f_{\text{orb}})^{11/5}}, \quad (17)$$

and therefore that the chirp mass uncertainty is

$$\left(\frac{\Delta\mathcal{M}_c}{\mathcal{M}_c} \right)^2 = \left(\frac{11}{5} \frac{\Delta f_{\text{orb}}}{f_{\text{orb}}} \right)^2 + \left(\frac{3}{5} \frac{\Delta \dot{f}_{\text{orb}}}{\dot{f}_{\text{orb}}} \right)^2 + \left(\frac{3}{5} \frac{\Delta F(e)}{F(e)} \right)^2. \quad (18)$$

We calculate the frequency uncertainties using Takahashi & Seto (2002), such that

$$\frac{\Delta f_{\text{orb}}}{f_{\text{orb}}} = 4\sqrt{3} \cdot \frac{1}{\rho} \frac{1}{T_{\text{obs}}} \frac{1}{f_{\text{orb}}}, \quad (19)$$

$$\frac{\Delta \dot{f}_{\text{orb}}}{\dot{f}_{\text{orb}}} = 6\sqrt{5} \cdot \frac{1}{\rho} \left(\frac{1}{T_{\text{obs}}} \right)^2 \frac{1}{\dot{f}_{\text{orb}}}, \quad (20)$$

where ρ is the signal-to-noise ratio and T_{obs} is the LISA mission length. Then we calculate the eccentricity certainty as discussed in Sec. 3.4.1 and propagate it so that

$$\frac{\Delta F(e)}{F(e)} = \Delta e \cdot \frac{(1256 + 1608e^2 + 111e^4)e}{96 + 196e^2 - 255e^4 - 37e^6}. \quad (21)$$

We use Eq. 18 to calculate the chirp mass uncertainty for each DCO in our sample and plot it in the lower centre panel of Fig. 4. We show the distribution as a CDF that is normalised to the expected number of detections to better indicate the absolute number of detections that will have well determined chirp masses. We find that approximately 10 BHBHs, 10 BHNSs and 5 NSNSs have measurable chirp masses (as indicated by the shaded region). We emphasise that this is a pessimistic estimate due to the pessimistic nature of how we determine the eccentricity uncertainty.

3.4.3. Sky localisation

We quantify the sky localisation of a source by calculating its angular resolution. Since we find that all potential sources are stationary on the timescale of the LISA mission, following Mandel et al. (2018), we can use the timing accuracy of LISA and the effective detector baseline to calculate the angular resolution, σ_θ , as

$$\sigma_\theta = 16.6^\circ \left(\frac{7}{\rho} \right) \left(\frac{5 \times 10^{-4} \text{ Hz}}{f_{\text{dom}}} \right) \left(\frac{2 \text{ AU}}{L} \right), \quad (22)$$

where ρ is the signal-to-noise ratio, f_{dom} is the harmonic frequency with the strongest signal-to-noise ratio ($f_{\text{dom}} = n_{\text{dom}} f_{\text{orb}}$ and $n_{\text{dom}} = 2$ for circular binaries) and L is the effective detector baseline.

We plot the angular resolution in the last panel of Fig. 4 as a CDF normalised to the expected detection rate of each DCO. From this plot, we see that the majority of sources can be resolved to an angular resolution of 10 square degrees. The size of a pencil beam for a 15m diameter SKA dish observing at 1.4 GHz is roughly 0.67 square degrees, corresponding to an angular resolution of $\sigma_\theta = \sqrt{(0.67/\pi)} = 0.46^\circ$ (which, for intuition, is approximately the angular size of the moon). Applying this to the plot shows that about 20% of DCOs can be covered by a single pointing of SKA. We will discuss the prospects of matching LISA detections to radio pulsars with SKA further in Sec. 4.2.

3.5. Model variations

[TODO: This will be about how the shapes of the parameter distributions change for the different model variations]

4. DISCUSSION

4.1. Identification of GW sources

It is important to note that, though we present predictions for the detection rates of specific DCO types, the nature of the source may not be immediately apparent from the gravitational wave signal.

4.1.1. Distinguishing from WDWD population

The population of Galactic WDWDs detectable with LISA will be several orders of magnitude larger than the more massive DCOs on which we focus in this paper (e.g. Korol et al. 2017). It is therefore imperative that we consider how to distinguish from this much more numerous population of sources.

The easiest way to check whether a source is a WDWD is to check its chirp mass. The mass of a non-rotating white dwarf cannot be larger than the Chandrasekhar limit of $1.44 M_\odot$ (Chandrasekhar 1931), so we can take

the maximum chirp mass of a WDWD to be $\sim 1.25 M_{\odot}$. Therefore, any DCO with a chirp mass that satisfies $M_c > 1.25 M_{\odot} + 2\Delta M_c$ must not be a WDWD. We find that 17%(23%) of BHBHs, 20%(24%) of BHNSs and 2.4%(2.5%) of NSNSs for a 4(10)-year LISA mission satisfy this condition.

[TODO: Another bit about the fact that eccentric DCOs that are resolved within the disc can be quite confidently confirmed as not WDWDs]

4.1.2. Separating BHBHs, BHNSs and NSNSs

[TODO:]

4.2. Matching LISA detections to pulsars with SKA

Since the vast majority of the LISA detectable population of DCOs will not merge for many years, the main form of electromagnetic counterpart for this population is pulsars. Therefore, for this section we focus only on BHNSs and NSNSs since no BHBH system will contain a pulsar. The joint detection of a binary pulsar with LISA and SKA would not only help to constrain the parameters of the binary, but also enable investigation of other compact object physics. A pulsar(PSR)+BH can be provide stringent tests of theories of gravity, in particular the “No-hair theorem” (Keane et al. 2015). Alternatively, an ultrarelativistic PSR+NS system could be used to measure the neutron star equation of state up to an order of magnitude better than other proposed observations (Kyutoku et al. 2019; Thrane et al. 2020).

In this section, we perform some back-of-the-envelope calculations to order to estimate how we can use SKA to match pulsars to LISA detections.

First, we can consider how many pulsars SKA is likely to detect. Keane et al. (2015) uses PSRPOPpy (Bates et al. 2014) to simulate the Milky Way pulsar population. They find that for SKA-1, approximately 10000 pulsars will be discovered. The second phase of SKA, which should also have been approved and be in operation by the time of the LISA mission, would yield a total of 35000-41000 pulsars (Keane et al. 2015), where we use the average, 38000, in further estimates below. Moreover, we are only interested in pulsars that are part of a binary system. We can estimate this pulsar binary fraction as the fraction of known pulsars that are in binaries using the ATNF Pulsar Catalogue⁸ (Manchester et al. 2005). 290 of the 2872 currently known pulsars are in binary systems and thus we can estimate the binary fraction of pulsars as 10%.

Next, we can find the total number of pulsars SKA will detect in a patch on the sky. The total sky area that the

SKA mission covers is approximately 7200 deg^2 , which is calculated by integrating over the sky for all Galactic longitudes and Galactic latitudes limited to $|b| < 10^\circ$, which are the limits on SKA-mid (Keane et al. 2015). If we assume that the pulsars are found uniformly across the sky, this means that roughly 0.14 and 0.49-0.57 binary pulsars are expected per square degree for SKA-1 and SKA-2 respectively. Note that the assumption assumption of a uniform distribution is not realistic as pulsars will tend to be far more concentrated in the Galactic centre but we use it to provide an upper bound on these estimates.

Alternatively, we could write that we expect a single pulsar per 7.2 deg^2 and $2.1\text{-}1.8 \text{ deg}^2$ for SKA-1 and SKA-2 respectively, which corresponds to angular resolutions of $\sigma_\theta = 1.51^\circ$ and $\sigma_\theta = 0.82\text{-}0.76^\circ$. Given these estimates, and by considering the last panel of Fig. 4, approximately 10 and 6 (for SKA-1 and SKA-2) DCOs containing NSs will be localised well enough such that, if the NS is a pulsar, SKA can unambiguously match it to the radio signal.

If there is more than one pulsar in the region given by the LISA sky localisation, one can compare the measured parameters of the system in LISA and SKA. Both SKA and LISA will measure the orbital frequency to high precision, as well as the time derivative of the frequency and chirp mass to a lesser precision, of each of these systems. Therefore, one could perform a targeted search with SKA that checks the sky location given by LISA and only looking for binary pulsars with orbital frequencies within the errors. If there was *still* more than one possible pulsar one could then also check against the chirp mass. In this way, it would still be possible to get a joint detection between SKA and LISA even when the sky area implied by the LISA detection contains more than one pulsar.

In order to assess the efficacy of this method, we would need to know the probability that two random binary pulsars would have orbital frequencies and chirp masses close enough that one could not tell which pulsar matches the LISA detection. This would require simulating the SKA population of pulsars with a code such as PSRPOPpy to find the frequency and chirp mass distribution and thus is beyond the scope of this paper. However, the uncertainty on the orbital frequency of a binary on the detection threshold ($\rho = 7$) for a 4-year LISA mission is $2.5 \times 10^{-9} \text{ Hz}$ and $1.0 \times 10^{-9} \text{ Hz}$ for a 10-year mission (calculated using Eq. 19). Therefore, we expect that SKA could likely isolate the correct binary pulsar to match to a LISA detection even when several are present in the sky localisation region.

⁸<https://www.atnf.csiro.au/research/pulsar/psrcat>

4.3. Caveats

Population synthesis limitations: As with any study involving a population synthesis code, our results rely on uncertain stellar physics and the use of approximate fitting formulae. We cannot use detailed stellar evolution codes to produce such a large sample of DCOs in a reasonable amount of time. Therefore COMPAS uses fitting formulae and approximate prescriptions based on (sometimes limited) grids of detailed models to describe the evolution of binary stars. This means that some of the finer points of evolution may be approximated but generally the final product of the stars on a population as a whole is reasonably close to the true result. In addition, much of the underlying physics is uncertain, such as the common envelope evolution and mass transfer physics. We attempt to understand the importance of these assumptions by creating many different physics variations. However, it is not reasonable to change every possible parameter (especially since many parts of the code have fixed assumptions) and therefore our results are subject to the accuracy of the assumptions made within the COMPAS code.

Underlying helium star models: One major weakness is that the [Hurley et al. \(2000\)](#) fitting formulae for the evolution of helium stars are based on a grid of models from $0.3 M_{\odot}$ to $10 M_{\odot}$, for a single metallicity ($Z = 0.02$) and thus the formulae have no metallicity dependence and are extrapolated for higher masses. A more detailed set of models in this regime could lead to large changes in the evolution of naked helium stars, a common progenitor of DCOs, and thus affect the detection rate of DCOs.

Limited metallicity range: Another limitation of the stellar evolution fitting formulae that COMPAS uses is that they are limited to a metallicity range of $10^{-4} \leq Z \leq 0.03$ and should not be extrapolated outside this region. On the scale of the Universe (more relevant for LIGO predictions), this does not usually pose a significant problem as the population is usually fairly low metallicity. However, for local GW detection in the Milky Way (based on the metallicity relation in [Frankel et al. \(2018\)](#)), the metallicity distribution can extend as far as $10^{-5} \leq Z \leq 0.06$, with a significant fraction of formation occurs past $Z = 0.03$. Therefore, for our study we had to reassign any metallicities outside of COMPAS' range. For any metallicity below the minimum, we places it in our lowest metallicity bin. For any metallicity above the minimum we placed it uniformly randomly in one of the top 5 highest bins (since using a single bin for many binaries led to unphysical artifacts in our results).

Other formation channels: We also note that our findings are only the result of a single formation channel (isolated binary formation). We do not consider other channels such as dynamical formation or chemically homogeneous evolution, which could increase the detection rate and alter the parameter distributions. For instance, [Kremer et al. \(2018\)](#) showed that around 21 systems could be detected in Milky Way globular clusters through dynamical formation and thus different channels can still contribute significantly to the detection rate.

Halo and globular clusters: Moreover, our model for the Milky Way, though more extensive than many previous studies, does not consider the contributions from the Galactic halo or globular clusters. [Lamberts et al. \(2018\)](#) found that the halo's contribution to the detection rate was minimal and, since the metallicity distribution of the halo is uncertain, we did not include it in our galaxy model. The impact of globular clusters would have required a more detailed look into dynamical formation that was beyond the scope of this paper but we again highlight the work of [Kremer et al. \(2018\)](#) that investigated these rates.

Systemic kicks: Another important consideration about our galaxy is that we do not include the effect of systemic kicks on the final location of the sources. This would require integrating the orbital evolution of the millions of binaries in our sample and thus was not computationally reasonable to include. We investigated the effect of kicks for a small grid of binaries and found that though they would result in a more spread out distribution within the galaxy (with a smaller concentration in the galaxy centre), the overall distribution of positions would be relatively unchanged and very few sources have strong enough kicks to reach escape velocity for the Milky Way.

Eccentricity measurement uncertainty: As noted in Sec. 3.4.1, the method that we use to determine the eccentricity uncertainty is pessimistic as it requires each harmonic to be individually detectable. In reality this may not be necessary depending on the efficacy of matched-filter analysis of LISA data. For an eccentric source to have been detected within the LISA data, several harmonics would already have to have been matched as the same source. This could be done by looking in the same region of the sky for signals with similar chirp masses and distances to the most detectable harmonic in order to find other harmonics that are below the regular detection threshold. This would allow one to refine the measurement of the eccentricity uncertainty much further by comparing the many different harmonics. Therefore, the eccentricity uncertainty that we calculate in

this study is a pessimistic estimate. Smaller eccentricity uncertainties would have two main effects on our results. Firstly, the chirp mass error would decrease slightly in the cases where it is dominated by the eccentricity uncertainty, however it is mainly dominated by the frequency derivative uncertainty since most sources are essentially stationary and so have extremely small chirps. Secondly, it would improve our ability to distinguish between WD-WDs and these higher mass DCOs. However, until we know more about how LISA will search for eccentric sources, we rely upon our pessimistic estimates.

5. COMPARISON WITH PREVIOUS STUDIES

In Figure 5, we compare similar previous studies that have investigated the population of stellar mass BHBHs, BHNSs and NSNSs that are detectable with LISA. The table details the expected detection rates predicted by each paper as well as their assumptions regarding their Milky Way galaxy model, binary population synthesis simulation and LISA mission specifications. This table not include the number papers on the LISA WDWD population as we do not make predictions for these DCOs.

In a seminal work, Nelemans et al. (2001) were the first to investigate the population of LISA detectable stellar mass double compact objects. Their predictions of the number of detectable DCOs are very different from our own, where we find a significantly higher detection rate for BHBHs and BHNSs, as well as a slightly lower rate for NSNSs. However, since their paper, there have been many changes both to the specifications of LISA (such as the mission length and SNR threshold for detection) and our understanding of massive star evolution, which likely strongly affect the expected detections rates.

Belczynski et al. (2010a) built upon this work by using a different population synthesis code with two model variations and a multi-component model for the Milky Way. They found a similar number of BHBH and BHNS detection to Nelemans et al. (2001), but a lower number of NSNS detections. The low total detection rate for all DCOs in this paper is unsurprising given the relatively high SNR threshold of 10 and short mission length of 1 year. The reduced mission length means that the source signal has much less time to accumulate, whilst many fewer WDWDs can be resolved in this time, leading to a weaker signal and an increased Galactic confusion noise relative to our work.

More recently, Lamberts et al. (2018) presented a new approach to the problem by using the FIRE simulation (Hopkins et al. 2014) to distribute their sources rather than an analytical model of the Milky Way, thus being the first paper in this area to incorporate metallicity

dependence into their Milky Way model. Sesana et al. (2020) followed up on this paper using the same simulated BHBH population and presented updated results for the number of expected BHBH detections. They find significantly fewer BHBHs than our fiducial model despite using the same SNR threshold and LISA mission length.

The discrepancy between their results and ours could be a result of different implicit assumptions in their population synthesis code, however we expect that BSE should be similar to COMPAS since it provided the basis of the COMPAS code. Another major difference is that, unlike this work, they assume that all binaries are circular for the purpose of detection in LISA, which could result in a lower number of detections by missing eccentric binaries that appear as weaker signals when assumed to be circular. We also improve upon this work by using a larger number of metallicity bins since a low number of metallicity bins can produce artificial features in the mass distribution of DCOs and possibly affect the detection rate [TODO: needs citation, perhaps @Stephen knows?].

Lau et al. (2020) investigated the number of Galactic NSNS binaries that could be detected by LISA. Their study uses the same population synthesis code, COMPAS, as this work, though an earlier version. Despite this, their study found a much larger number of detections. They make several different physical assumptions in their population synthesis, using the Fryer et al. (2012) rapid remnant mass prescription, limiting the maximum neutron star mass to $2 M_{\odot}$ and not implementing PISN. However, we note that none of these assumptions significantly affect the NSNS LISA detection rate (see bottom panel of Fig. 3, models L, M and O).

We therefore surmise that the difference between our results is likely due to way in which we simulate the Milky Way. Lau et al. (2020) assumes constant star formation, solar metallicity and distributes binaries without any considerations of the chemical enrichment history of the Milky Way, whilst we use the distributions from Frankel et al. (2018) for the star formation rate, metallicity and positions. The Frankel et al. (2018) star formation rate decreases over time and the metallicity distribution peaks above solar metallicity, both changes that could decrease the NSNS detection rate given that we find most NSNS binaries in our sample have short inspiral times compared to the age of the Milky Way and higher metallicity would lead to increased stellar winds and hence less massive DCOs.

Finally, Breivik et al. (2020) introduced the population synthesis code COSMIC and presented detections for many different DCO types in LISA using this code.

[TODO: what I write here will depend how much the numbers change in upcoming run. Long story short is that they only have two metallicity bins and use the optimistic CE model.].

6. CONCLUSION & SUMMARY

Software: COMPAS (version 02.12.00) <http://github.com/TeamCOMPAS/COMPAS>. (Stevenson et al. 2017; Vigna-Gómez et al. 2018; Broekgaarden et al. 2019), Python available from python.org, matplotlib (Hunter 2007), NumPy (van der Walt et al. 2011), Astropy (<http://www.astropy.org> Astropy Collaboration et al. 2013, 2018).

ACKNOWLEDGMENTS

We thank Mike Lau, Floris Kummer, Eva Laplace, Rob Farmer, Katie Sharpe, Mathieu Renzo, Katie Brevis, Alberto Sesana, Valeriya Korol, Will Farr and the members of the COMPAS collaboration for insightful discussions. This project was funded in part by the European Union’s Horizon 2020 research and innovation program from the European Research Council (ERC, Grant agreement No. 715063), and by the Netherlands Organization for Scientific Research (NWO) as part of the Vidi research program BinWaves with project number 639.042.728. We further acknowledge the Black Hole Initiative funded by a generous contribution of the John Templeton Foundation and the Gordon and Betty Moore Foundation.

Author	Year	DCO Predictions			Population Synthesis					
		BHBH	BHNS	NSNS	Code	Open Source Code	Metallicity		Binary Physics Variations	
Wagg	2021	25.9, 42.0	26.7, 44.5	11.3, 19.3	COMPAS	✓	50 bins between [1e-4, 3e-2]		15	
Sesana	2020	4.2, 6.5	X	X	BSE	✓	13 bins between [1e-4, 3e-2]		None	
Breivik	2020	93	33	8	COSMIC	✓	0.02, 0.003		None	
Lau	2020	X	X	35	COMPAS	✓	0.0142		Case BB always unstable, Single SN, alpha=0.1	
Lamberts	2018	25	X	X	BSE	✓	13 bins between [1e-4, 3e-2]		None	
Liu	2014	6	3	16	BSE	✓	0.02		None	
Belczynski	2010	2.3, 0	0.2, 0	4, 1.7	Startrack	X	0.02 (disc, bulge), 0.001 (halo)		Optimistic CE, Pessimistic CE	
Nelemans	2001	0	3	39	SeBa	X	0.02		None	

Author	Year	Galaxy and Positioning					Detection		
		Star formation history		Spatial distribution		Galactic Components	Metallicity Dependent Distributions	SNR Limit	LISA Mission Time
Wagg	2021	Exponential 8-0 Gyr ago (thin disc), Exponential 12-8 Gyr ago (thick disc), Skewed gaussian 0-6 Gyr (bulge)	Exponential radial and vertical, scale length/height for each component, thin disc has inside-out growth	Thin disc, thick disc, bulge	✓	7	4, 10	Full	
Sesana	2020	FIRE simulation	FIRE simulation	Everything within 300kpc	✓	7	4, 10	Used for evolution, ignored during detection	
Breivik	2020	Constant over 10 Gyr (thin disc), 1 Gyr burst 10 Gyr ago (bulge), 1 Gyr burst 11 Gyr (thick disc)	McMillan 2011	Thin disc, thick disc, bulge	X	7	4		Full
Lau	2020	Constant	Miyamoto & Nagai potential (disc), Wilkinson & Evans potential (halo)	Single disc or halo	X	8	4	Full	
Lamberts	2018	FIRE simulation	FIRE simulation	Everything within 300kpc	✓	5	4	Used for evolution, ignored during detection	
Liu	2014	Constant over 13.7 Gyr	Exponential radial, sech^2 vertical (Benacquista+2007)	Single disc	X	7	2		Assumed circular
Belczynski	2010	Constant over 10 Gyr (disc), 1 Gyr burst 10 Gyr ago (bulge), burst at 13 Gyr (halo)	Exponential sphere (bulge), exponential radial and vertical (disc), spherical shell (halo)	Disc, bulge, halo	X	10	1	Full	
Nelemans	2001	Exponential over 10 Gyr	Exponential radial, sech^2 vertical	Single disc	X	1, 5	1	Full	

Figure 5. A table comparing previous studies of a similar nature to this work. The works listed in the table are Nelemans et al. (2001); Belczynski et al. (2010a); Liu & Zhang (2014); Lamberts et al. (2018); Lau et al. (2020); Breivik et al. (2020); Sesana et al. (2020).

REFERENCES

- Abadie, J., Abbott, B. P., Abbott, R., et al. 2010, Classical and Quantum Gravity, 27, 173001, doi: [10.1088/0264-9381/27/17/173001](https://doi.org/10.1088/0264-9381/27/17/173001)
- Abbott, B. P., Abbott, R., Abbott, T. D., et al. 2016, Physical Review X, 6, 041015, doi: [10.1103/PhysRevX.6.041015](https://doi.org/10.1103/PhysRevX.6.041015)
- . 2019, Physical Review X, 9, 031040, doi: [10.1103/PhysRevX.9.031040](https://doi.org/10.1103/PhysRevX.9.031040)
- . 2020a, ApJL, 892, L3, doi: [10.3847/2041-8213/ab75f5](https://doi.org/10.3847/2041-8213/ab75f5)
- . 2017, PhRvL, 119, 161101, doi: [10.1103/PhysRevLett.119.161101](https://doi.org/10.1103/PhysRevLett.119.161101)
- Abbott, R., Abbott, T. D., Abraham, S., et al. 2020b, arXiv e-prints, arXiv:2010.14527. <https://arxiv.org/abs/2010.14527>
- . 2020c, ApJL, 896, L44, doi: [10.3847/2041-8213/ab960f](https://doi.org/10.3847/2041-8213/ab960f)
- . 2021, ApJL, 913, L7, doi: [10.3847/2041-8213/abe949](https://doi.org/10.3847/2041-8213/abe949)
- Abdul-Masih, M., Banyard, G., Bodensteiner, J., et al. 2020, Nature, 580, E11, doi: [10.1038/s41586-020-2216-x](https://doi.org/10.1038/s41586-020-2216-x)
- Abt, H. A. 1983, ARA&A, 21, 343, doi: [10.1146/annurev.aa.21.090183.002015](https://doi.org/10.1146/annurev.aa.21.090183.002015)
- Amaro-Seoane, P., Audley, H., Babak, S., et al. 2017, arXiv e-prints, arXiv:1702.00786. <https://arxiv.org/abs/1702.00786>
- Antonini, F., & Rasio, F. A. 2016, ApJ, 831, 187, doi: [10.3847/0004-637X/831/2/187](https://doi.org/10.3847/0004-637X/831/2/187)
- Antonini, F., Toonen, S., & Hamers, A. S. 2017, ApJ, 841, 77, doi: [10.3847/1538-4357/aa6f5e](https://doi.org/10.3847/1538-4357/aa6f5e)
- Astropy Collaboration, Price-Whelan, A. M., Sipőcz, B. M., et al. 2018, AJ, 156, 123, doi: [10.3847/1538-3881/aabc4f](https://doi.org/10.3847/1538-3881/aabc4f)
- Astropy Collaboration, Robitaille, T. P., Tollerud, E. J., et al. 2013, A&A, 558, A33, doi: [10.1051/0004-6361/201322068](https://doi.org/10.1051/0004-6361/201322068)
- Barack, L., & Cutler, C. 2004, PhRvD, 69, 082005, doi: [10.1103/PhysRevD.69.082005](https://doi.org/10.1103/PhysRevD.69.082005)
- Bates, S. D., Lorimer, D. R., Rane, A., & Swiggum, J. 2014, MNRAS, 439, 2893, doi: [10.1093/mnras/stu157](https://doi.org/10.1093/mnras/stu157)
- Begelman, M. C., Blandford, R. D., & Rees, M. J. 1980, Nature, 287, 307, doi: [10.1038/287307a0](https://doi.org/10.1038/287307a0)
- Belczynski, K., Benacquista, M., & Bulik, T. 2010a, ApJ, 725, 816, doi: [10.1088/0004-637X/725/1/816](https://doi.org/10.1088/0004-637X/725/1/816)
- Belczynski, K., Bulik, T., Fryer, C. L., et al. 2010b, ApJ, 714, 1217, doi: [10.1088/0004-637X/714/2/1217](https://doi.org/10.1088/0004-637X/714/2/1217)
- Belczynski, K., Holz, D. E., Bulik, T., & O’Shaughnessy, R. 2016, Nature, 534, 512, doi: [10.1038/nature18322](https://doi.org/10.1038/nature18322)
- Belczynski, K., Kalogera, V., Rasio, F. A., et al. 2008, ApJS, 174, 223, doi: [10.1086/521026](https://doi.org/10.1086/521026)
- Belczynski, K., Taam, R. E., Kalogera, V., Rasio, F. A., & Bulik, T. 2007, ApJ, 662, 504, doi: [10.1086/513562](https://doi.org/10.1086/513562)
- Bertelli, G., Bressan, A., Chiosi, C., Fagotto, F., & Nasi, E. 1994, A&AS, 106, 275
- Blaauw, A. 1961, BAN, 15, 265
- Bolton, C. T. 1972, Nature, 235, 271, doi: [10.1038/235271b0](https://doi.org/10.1038/235271b0)
- Bovy, J., Leung, H. W., Hunt, J. A. S., et al. 2019, MNRAS, 490, 4740, doi: [10.1093/mnras/stz2891](https://doi.org/10.1093/mnras/stz2891)
- Bovy, J., Rix, H.-W., Schlafly, E. F., et al. 2016, ApJ, 823, 30, doi: [10.3847/0004-637X/823/1/30](https://doi.org/10.3847/0004-637X/823/1/30)
- Breivik, K., Coughlin, S., Zevin, M., et al. 2020, ApJ, 898, 71, doi: [10.3847/1538-4357/ab9d85](https://doi.org/10.3847/1538-4357/ab9d85)
- Breivik, K., Rodriguez, C. L., Larson, S. L., Kalogera, V., & Rasio, F. A. 2016, ApJL, 830, L18, doi: [10.3847/2041-8205/830/1/L18](https://doi.org/10.3847/2041-8205/830/1/L18)
- Broekgaarden, F. S., Berger, E., Neijssel, C. J., et al. 2021, arXiv e-prints, arXiv:2103.02608. <https://arxiv.org/abs/2103.02608>
- Broekgaarden, F. S., Justham, S., de Mink, S. E., et al. 2019, MNRAS, 490, 5228, doi: [10.1093/mnras/stz2558](https://doi.org/10.1093/mnras/stz2558)
- Chandrasekhar, S. 1931, ApJ, 74, 81, doi: [10.1086/143324](https://doi.org/10.1086/143324)
- Chattopadhyay, D., Stevenson, S., Hurley, J. R., Bailes, M., & Broekgaarden, F. 2020, arXiv e-prints, arXiv:2011.13503. <https://arxiv.org/abs/2011.13503>
- Corral-Santana, J. M., Casares, J., Muñoz-Darias, T., et al. 2016, A&A, 587, A61, doi: [10.1051/0004-6361/201527130](https://doi.org/10.1051/0004-6361/201527130)
- de Kool, M. 1990, ApJ, 358, 189, doi: [10.1086/168974](https://doi.org/10.1086/168974)
- de Mink, S. E., & Belczynski, K. 2015, ApJ, 814, 58, doi: [10.1088/0004-637X/814/1/58](https://doi.org/10.1088/0004-637X/814/1/58)
- de Mink, S. E., Cantiello, M., Langer, N., et al. 2009, A&A, 497, 243, doi: [10.1051/0004-6361/200811439](https://doi.org/10.1051/0004-6361/200811439)
- de Mink, S. E., & Mandel, I. 2016, MNRAS, 460, 3545, doi: [10.1093/mnras/stw1219](https://doi.org/10.1093/mnras/stw1219)
- Dewi, J. D. M., Pols, O. R., Savonije, G. J., & van den Heuvel, E. P. J. 2002, MNRAS, 331, 1027, doi: [10.1046/j.1365-8711.2002.05257.x](https://doi.org/10.1046/j.1365-8711.2002.05257.x)
- du Buisson, L., Marchant, P., Podsiadlowski, P., et al. 2020, MNRAS, 499, 5941, doi: [10.1093/mnras/staa3225](https://doi.org/10.1093/mnras/staa3225)
- Eichler, D., Livio, M., Piran, T., & Schramm, D. N. 1989, Nature, 340, 126, doi: [10.1038/340126a0](https://doi.org/10.1038/340126a0)
- El-Badry, K., & Quataert, E. 2020, MNRAS, 493, L22, doi: [10.1093/mnrasl/slaa004](https://doi.org/10.1093/mnrasl/slaa004)
- Eldridge, J. J., Stanway, E. R., Breivik, K., et al. 2020, MNRAS, 495, 2786, doi: [10.1093/mnras/staa1324](https://doi.org/10.1093/mnras/staa1324)
- Farmer, R., Renzo, M., de Mink, S. E., Marchant, P., & Justham, S. 2019, ApJ, 887, 53, doi: [10.3847/1538-4357/ab518b](https://doi.org/10.3847/1538-4357/ab518b)
- Farr, W. M., Sravan, N., Cantrell, A., et al. 2011, ApJ, 741, 103, doi: [10.1088/0004-637X/741/2/103](https://doi.org/10.1088/0004-637X/741/2/103)
- Finn, L. S., & Thorne, K. S. 2000, PhRvD, 62, 124021, doi: [10.1103/PhysRevD.62.124021](https://doi.org/10.1103/PhysRevD.62.124021)

- Frankel, N., Rix, H.-W., Ting, Y.-S., Ness, M., & Hogg, D. W. 2018, ApJ, 865, 96, doi: [10.3847/1538-4357/aadba5](https://doi.org/10.3847/1538-4357/aadba5)
- Fryer, C. L., Belczynski, K., Ramirez-Ruiz, E., et al. 2015, ApJ, 812, 24, doi: [10.1088/0004-637X/812/1/24](https://doi.org/10.1088/0004-637X/812/1/24)
- Fryer, C. L., Belczynski, K., Wiktorowicz, G., et al. 2012, ApJ, 749, 91, doi: [10.1088/0004-637X/749/1/91](https://doi.org/10.1088/0004-637X/749/1/91)
- Gerosa, D., Ma, S., Wong, K. W. K., et al. 2019, PhRvD, 99, 103004, doi: [10.1103/PhysRevD.99.103004](https://doi.org/10.1103/PhysRevD.99.103004)
- Gompertz, B. P., Levan, A. J., & Tanvir, N. R. 2020, ApJ, 895, 58, doi: [10.3847/1538-4357/ab8d24](https://doi.org/10.3847/1538-4357/ab8d24)
- Hamann, W. R., Gräfener, G., Liermann, A., et al. 2019, A&A, 625, A57, doi: [10.1051/0004-6361/201834850](https://doi.org/10.1051/0004-6361/201834850)
- Heuvel, E. P. J. V. D. 2011, Compact stars and the evolution of binary systems (World Scientific Publishing Co. Pte. Ltd), 55–73, doi: [10.1142/9789814374774_0006](https://doi.org/10.1142/9789814374774_0006)
- Hjellming, M. S., & Webbink, R. F. 1987, ApJ, 318, 794, doi: [10.1086/165412](https://doi.org/10.1086/165412)
- Hobbs, G., Lorimer, D. R., Lyne, A. G., & Kramer, M. 2005, MNRAS, 360, 974, doi: [10.1111/j.1365-2966.2005.09087.x](https://doi.org/10.1111/j.1365-2966.2005.09087.x)
- Hopkins, P. F., Kereš, D., Oñorbe, J., et al. 2014, MNRAS, 445, 581, doi: [10.1093/mnras/stu1738](https://doi.org/10.1093/mnras/stu1738)
- Hotokezaka, K., Nissanke, S., Hallinan, G., et al. 2016, ApJ, 831, 190, doi: [10.3847/0004-637X/831/2/190](https://doi.org/10.3847/0004-637X/831/2/190)
- Hulse, R. A., & Taylor, J. H. 1975, ApJL, 195, L51, doi: [10.1086/181708](https://doi.org/10.1086/181708)
- Hunter, J. D. 2007, Computing in Science and Engineering, 9, 90, doi: [10.1109/MCSE.2007.55](https://doi.org/10.1109/MCSE.2007.55)
- Hurley, J. R., Pols, O. R., & Tout, C. A. 2000, MNRAS, 315, 543, doi: [10.1046/j.1365-8711.2000.03426.x](https://doi.org/10.1046/j.1365-8711.2000.03426.x)
- Hurley, J. R., Tout, C. A., & Pols, O. R. 2002, MNRAS, 329, 897, doi: [10.1046/j.1365-8711.2002.05038.x](https://doi.org/10.1046/j.1365-8711.2002.05038.x)
- Ivanova, N., Heinke, C. O., Rasio, F. A., Belczynski, K., & Fregeau, J. M. 2008, MNRAS, 386, 553, doi: [10.1111/j.1365-2966.2008.13064.x](https://doi.org/10.1111/j.1365-2966.2008.13064.x)
- Ivanova, N., & Taam, R. E. 2004, ApJ, 601, 1058, doi: [10.1086/380561](https://doi.org/10.1086/380561)
- Kalogera, V., & Baym, G. 1996, ApJL, 470, L61, doi: [10.1086/310296](https://doi.org/10.1086/310296)
- Kalogera, V., Belczynski, K., Kim, C., O’Shaughnessy, R., & Willems, B. 2007, PhR, 442, 75, doi: [10.1016/j.physrep.2007.02.008](https://doi.org/10.1016/j.physrep.2007.02.008)
- Keane, E., Bhattacharyya, B., Kramer, M., et al. 2015, in Advancing Astrophysics with the Square Kilometre Array (AASKA14), 40. <https://arxiv.org/abs/1501.00056>
- Klein, A., Barausse, E., Sesana, A., et al. 2016, PhRvD, 93, 024003, doi: [10.1103/PhysRevD.93.024003](https://doi.org/10.1103/PhysRevD.93.024003)
- Korol, V., Rossi, E. M., & Barausse, E. 2019, MNRAS, 483, 5518, doi: [10.1093/mnras/sty3440](https://doi.org/10.1093/mnras/sty3440)
- Korol, V., Rossi, E. M., Groot, P. J., et al. 2017, MNRAS, 470, 1894, doi: [10.1093/mnras/stx1285](https://doi.org/10.1093/mnras/stx1285)
- Korol, V., & Safarzadeh, M. 2021, MNRAS, 502, 5576, doi: [10.1093/mnras/stab310](https://doi.org/10.1093/mnras/stab310)
- Korol, V., Toonen, S., Klein, A., et al. 2020, A&A, 638, A153, doi: [10.1051/0004-6361/202037764](https://doi.org/10.1051/0004-6361/202037764)
- Kreidberg, L., Bailyn, C. D., Farr, W. M., & Kalogera, V. 2012, ApJ, 757, 36, doi: [10.1088/0004-637X/757/1/36](https://doi.org/10.1088/0004-637X/757/1/36)
- Kremer, K., Chatterjee, S., Breivik, K., et al. 2018, PhRvL, 120, 191103, doi: [10.1103/PhysRevLett.120.191103](https://doi.org/10.1103/PhysRevLett.120.191103)
- Kroupa, P. 2001, MNRAS, 322, 231, doi: [10.1046/j.1365-8711.2001.04022.x](https://doi.org/10.1046/j.1365-8711.2001.04022.x)
- Kruckow, M. U., Tauris, T. M., Langer, N., Kramer, M., & Izzard, R. G. 2018, MNRAS, 481, 1908, doi: [10.1093/mnras/sty2190](https://doi.org/10.1093/mnras/sty2190)
- Kupfer, T., Korol, V., Shah, S., et al. 2018, MNRAS, 480, 302, doi: [10.1093/mnras/sty1545](https://doi.org/10.1093/mnras/sty1545)
- Kyutoku, K., Kiuchi, K., Sekiguchi, Y., Shibata, M., & Taniguchi, K. 2018, PhRvD, 97, 023009, doi: [10.1103/PhysRevD.97.023009](https://doi.org/10.1103/PhysRevD.97.023009)
- Kyutoku, K., Nishino, Y., & Seto, N. 2019, MNRAS, 483, 2615, doi: [10.1093/mnras/sty3322](https://doi.org/10.1093/mnras/sty3322)
- Lamberts, A., Blunt, S., Littenberg, T. B., et al. 2019, MNRAS, 490, 5888, doi: [10.1093/mnras/stz2834](https://doi.org/10.1093/mnras/stz2834)
- Lamberts, A., Garrison-Kimmel, S., Hopkins, P. F., et al. 2018, MNRAS, 480, 2704, doi: [10.1093/mnras/sty2035](https://doi.org/10.1093/mnras/sty2035)
- Lau, M. Y. M., Mandel, I., Vigna-Gómez, A., et al. 2020, MNRAS, 492, 3061, doi: [10.1093/mnras/staa002](https://doi.org/10.1093/mnras/staa002)
- Licquia, T. C., & Newman, J. A. 2015, ApJ, 806, 96, doi: [10.1088/0004-637X/806/1/96](https://doi.org/10.1088/0004-637X/806/1/96)
- Liu, J. 2009, MNRAS, 400, 1850, doi: [10.1111/j.1365-2966.2009.15574.x](https://doi.org/10.1111/j.1365-2966.2009.15574.x)
- Liu, J., Zhang, H., Howard, A. W., et al. 2019, Nature, 575, 618, doi: [10.1038/s41586-019-1766-2](https://doi.org/10.1038/s41586-019-1766-2)
- Liu, J., & Zhang, Y. 2014, PASP, 126, 211, doi: [10.1086/675721](https://doi.org/10.1086/675721)
- Lyne, A. G., & Lorimer, D. R. 1994, Nature, 369, 127, doi: [10.1038/369127a0](https://doi.org/10.1038/s41586-019-1766-2)
- Majewski, S. R., Schiavon, R. P., Frinchaboy, P. M., et al. 2017, AJ, 154, 94, doi: [10.3847/1538-3881/aa784d](https://doi.org/10.3847/1538-3881/aa784d)
- Manchester, R. N., Hobbs, G. B., Teoh, A., & Hobbs, M. 2005, AJ, 129, 1993, doi: [10.1086/428488](https://doi.org/10.1086/428488)
- Mandel, I., Sesana, A., & Vecchio, A. 2018, Classical and Quantum Gravity, 35, 054004, doi: [10.1088/1361-6382/aaa7e0](https://doi.org/10.1088/1361-6382/aaa7e0)
- Marchant, P., Langer, N., Podsiadlowski, P., Tauris, T. M., & Moriya, T. J. 2016, A&A, 588, A50, doi: [10.1051/0004-6361/201628133](https://doi.org/10.1051/0004-6361/201628133)
- Marchant, P., Renzo, M., Farmer, R., et al. 2019, ApJ, 882, 36, doi: [10.3847/1538-4357/ab3426](https://doi.org/10.3847/1538-4357/ab3426)

- Margalit, B., & Metzger, B. D. 2017, ApJL, 850, L19, doi: [10.3847/2041-8213/aa991c](https://doi.org/10.3847/2041-8213/aa991c)
- Massevitch, A., & Yungelson, L. 1975, Mem. Soc. Astron. Italiana, 46, 217
- McKernan, B., Ford, K. E. S., & O'Shaughnessy, R. 2020, MNRAS, 498, 4088, doi: [10.1093/mnras/staa2681](https://doi.org/10.1093/mnras/staa2681)
- McMillan, P. J. 2011, MNRAS, 414, 2446, doi: [10.1111/j.1365-2966.2011.18564.x](https://doi.org/10.1111/j.1365-2966.2011.18564.x)
- Metzger, B. D. 2017, Living Reviews in Relativity, 20, 3, doi: [10.1007/s41114-017-0006-z](https://doi.org/10.1007/s41114-017-0006-z)
- Miller, M. C., & Lauburg, V. M. 2009, ApJ, 692, 917, doi: [10.1088/0004-637X/692/1/917](https://doi.org/10.1088/0004-637X/692/1/917)
- Miller-Jones, J. C. A., Bahramian, A., Orosz, J. A., et al. 2021, Science, 371, 1046, doi: [10.1126/science.abb3363](https://doi.org/10.1126/science.abb3363)
- Morris, M. 1993, ApJ, 408, 496, doi: [10.1086/172607](https://doi.org/10.1086/172607)
- Narayan, R., Piran, T., & Shemi, A. 1991, ApJL, 379, L17, doi: [10.1086/186143](https://doi.org/10.1086/186143)
- Nelemans, G., Yungelson, L. R., & Portegies Zwart, S. F. 2001, A&A, 375, 890, doi: [10.1051/0004-6361:20010683](https://doi.org/10.1051/0004-6361:20010683)
- Nishizawa, A., Berti, E., Klein, A., & Sesana, A. 2016, PhRvD, 94, 064020, doi: [10.1103/PhysRevD.94.064020](https://doi.org/10.1103/PhysRevD.94.064020)
- Nissanke, S., Vallisneri, M., Nelemans, G., & Prince, T. A. 2012, ApJ, 758, 131, doi: [10.1088/0004-637X/758/2/131](https://doi.org/10.1088/0004-637X/758/2/131)
- Nomoto, K. 1984, ApJ, 277, 791, doi: [10.1086/161749](https://doi.org/10.1086/161749)
- . 1987, ApJ, 322, 206, doi: [10.1086/165716](https://doi.org/10.1086/165716)
- Öpik, E. 1924, Publications of the Tartu Astrofizica Observatory, 25, 1
- Özel, F., Psaltis, D., Narayan, R., & McClintock, J. E. 2010, ApJ, 725, 1918, doi: [10.1088/0004-637X/725/2/1918](https://doi.org/10.1088/0004-637X/725/2/1918)
- Paczyński, B., & Sienkiewicz, R. 1972, AcA, 22, 73
- Peters, P. C. 1964, Physical Review, 136, 1224, doi: [10.1103/PhysRev.136.B1224](https://doi.org/10.1103/PhysRev.136.B1224)
- Peters, P. C., & Mathews, J. 1963, Physical Review, 131, 435, doi: [10.1103/PhysRev.131.435](https://doi.org/10.1103/PhysRev.131.435)
- Pfahl, E., Podsiadlowski, P., & Rappaport, S. 2005, ApJ, 628, 343, doi: [10.1086/430515](https://doi.org/10.1086/430515)
- Pfahl, E., Rappaport, S., Podsiadlowski, P., & Spruit, H. 2002, ApJ, 574, 364, doi: [10.1086/340794](https://doi.org/10.1086/340794)
- Podsiadlowski, P., Langer, N., Poelarends, A. J. T., et al. 2004, ApJ, 612, 1044, doi: [10.1086/421713](https://doi.org/10.1086/421713)
- Pols, O. R., Schröder, K.-P., Hurley, J. R., Tout, C. A., & Eggleton, P. P. 1998, MNRAS, 298, 525, doi: [10.1046/j.1365-8711.1998.01658.x](https://doi.org/10.1046/j.1365-8711.1998.01658.x)
- Portegies Zwart, S. F., & McMillan, S. L. W. 2000, ApJL, 528, L17, doi: [10.1086/312422](https://doi.org/10.1086/312422)
- Robson, T., Cornish, N. J., & Liu, C. 2019, Classical and Quantum Gravity, 36, 105011, doi: [10.1088/1361-6382/ab1101](https://doi.org/10.1088/1361-6382/ab1101)
- Rodriguez, C. L., Amaro-Seoane, P., Chatterjee, S., & Rasio, F. A. 2018, PhRvL, 120, 151101, doi: [10.1103/PhysRevLett.120.151101](https://doi.org/10.1103/PhysRevLett.120.151101)
- Rodriguez, C. L., Morscher, M., Pattabiraman, B., et al. 2015, PhRvL, 115, 051101, doi: [10.1103/PhysRevLett.115.051101](https://doi.org/10.1103/PhysRevLett.115.051101)
- Ruiter, A. J., Belczynski, K., Benacquista, M., Larson, S. L., & Williams, G. 2010, ApJ, 717, 1006, doi: [10.1088/0004-637X/717/2/1006](https://doi.org/10.1088/0004-637X/717/2/1006)
- Sana, H., de Mink, S. E., de Koter, A., et al. 2012, Science, 337, 444, doi: [10.1126/science.1223344](https://doi.org/10.1126/science.1223344)
- Sellwood, J. A., & Binney, J. J. 2002, MNRAS, 336, 785, doi: [10.1046/j.1365-8711.2002.05806.x](https://doi.org/10.1046/j.1365-8711.2002.05806.x)
- Sesana, A. 2016, PhRvL, 116, 231102, doi: [10.1103/PhysRevLett.116.231102](https://doi.org/10.1103/PhysRevLett.116.231102)
- Sesana, A., Lamberts, A., & Petiteau, A. 2020, MNRAS, 494, L75, doi: [10.1093/mnrasl/slaa039](https://doi.org/10.1093/mnrasl/slaa039)
- Sharma, S., Hayden, M. R., & Bland-Hawthorn, J. 2020, arXiv e-prints, arXiv:2005.03646, <https://arxiv.org/abs/2005.03646>
- Shenar, T., Bodensteiner, J., Abdul-Masih, M., et al. 2020, A&A, 639, L6, doi: [10.1051/0004-6361/202038275](https://doi.org/10.1051/0004-6361/202038275)
- Shenar, T., Sablowski, D. P., Hainich, R., et al. 2019, A&A, 627, A151, doi: [10.1051/0004-6361/201935684](https://doi.org/10.1051/0004-6361/201935684)
- Sigurdsson, S., & Hernquist, L. 1993, Nature, 364, 423, doi: [10.1038/364423a0](https://doi.org/10.1038/364423a0)
- Silsbee, K., & Tremaine, S. 2017, ApJ, 836, 39, doi: [10.3847/1538-4357/aa5729](https://doi.org/10.3847/1538-4357/aa5729)
- Smarr, L. L., & Blandford, R. 1976, ApJ, 207, 574, doi: [10.1086/154524](https://doi.org/10.1086/154524)
- Snaith, O. N., Haywood, M., Di Matteo, P., et al. 2014, ApJL, 781, L31, doi: [10.1088/2041-8205/781/2/L31](https://doi.org/10.1088/2041-8205/781/2/L31)
- Soberman, G. E., Phinney, E. S., & van den Heuvel, E. P. J. 1997, A&A, 327, 620, <https://arxiv.org/abs/astro-ph/9703016>
- Srinivasan, G. 1989, A&A Rv, 1, 209, doi: [10.1007/BF00873079](https://doi.org/10.1007/BF00873079)
- Stephan, A. P., Naoz, S., Ghez, A. M., et al. 2016, MNRAS, 460, 3494, doi: [10.1093/mnras/stw1220](https://doi.org/10.1093/mnras/stw1220)
- Stevenson, S., Sampson, M., Powell, J., et al. 2019, ApJ, 882, 121, doi: [10.3847/1538-4357/ab3981](https://doi.org/10.3847/1538-4357/ab3981)
- Stevenson, S., Vigna-Gómez, A., Mandel, I., et al. 2017, Nature Communications, 8, 14906, doi: [10.1038/ncomms14906](https://doi.org/10.1038/ncomms14906)
- Taam, R. E., & Sandquist, E. L. 2000, ARA&A, 38, 113, doi: [10.1146/annurev.astro.38.1.113](https://doi.org/10.1146/annurev.astro.38.1.113)
- Takahashi, R., & Seto, N. 2002, ApJ, 575, 1030, doi: [10.1086/341483](https://doi.org/10.1086/341483)
- Tauris, T. M., Kramer, M., Freire, P. C. C., et al. 2017, ApJ, 846, 170, doi: [10.3847/1538-4357/aa7e89](https://doi.org/10.3847/1538-4357/aa7e89)

- Tauris, T. M., Langer, N., Moriya, T. J., et al. 2013, ApJL, 778, L23, doi: [10.1088/2041-8205/778/2/L23](https://doi.org/10.1088/2041-8205/778/2/L23)
- Tauris, T. M., Langer, N., & Podsiadlowski, P. 2015, MNRAS, 451, 2123, doi: [10.1093/mnras/stv990](https://doi.org/10.1093/mnras/stv990)
- Thrane, E., Oslowski, S., & Lasky, P. D. 2020, MNRAS, 493, 5408, doi: [10.1093/mnras/staa593](https://doi.org/10.1093/mnras/staa593)
- Timmes, F. X., Woosley, S. E., & Weaver, T. A. 1996, ApJ, 457, 834, doi: [10.1086/176778](https://doi.org/10.1086/176778)
- Tout, C. A., Pols, O. R., Eggleton, P. P., & Han, Z. 1996, MNRAS, 281, 257, doi: [10.1093/mnras/281.1.257](https://doi.org/10.1093/mnras/281.1.257)
- Tutukov, A., & Yungelson, L. 1973, Nauchnye Informatsii, 27, 70
- Tutukov, A. V., & Yungelson, L. R. 1993, MNRAS, 260, 675, doi: [10.1093/mnras/260.3.675](https://doi.org/10.1093/mnras/260.3.675)
- van der Walt, S., Colbert, S. C., & Varoquaux, G. 2011, Computing in Science and Engineering, 13, 22, doi: [10.1109/MCSE.2011.37](https://doi.org/10.1109/MCSE.2011.37)
- Vigna-Gómez, A., Neijssel, C. J., Stevenson, S., et al. 2018, MNRAS, 481, 4009, doi: [10.1093/mnras/sty2463](https://doi.org/10.1093/mnras/sty2463)
- Vink, J. S. 2017, A&A, 607, L8, doi: [10.1051/0004-6361/201731902](https://doi.org/10.1051/0004-6361/201731902)
- Vink, J. S., de Koter, A., & Lamers, H. J. G. L. M. 2000, A&A, 362, 295. <https://arxiv.org/abs/astro-ph/0008183>
- . 2001, A&A, 369, 574, doi: [10.1051/0004-6361:20010127](https://doi.org/10.1051/0004-6361:20010127)
- Webbink, R. F. 1984, ApJ, 277, 355, doi: [10.1086/161701](https://doi.org/10.1086/161701)
- Webster, B. L., & Murdin, P. 1972, Nature, 235, 37, doi: [10.1038/235037a0](https://doi.org/10.1038/235037a0)
- Woosley, S. E., Blinnikov, S., & Heger, A. 2007, Nature, 450, 390, doi: [10.1038/nature06333](https://doi.org/10.1038/nature06333)
- Xu, X.-J., & Li, X.-D. 2010a, ApJ, 716, 114, doi: [10.1088/0004-637X/716/1/114](https://doi.org/10.1088/0004-637X/716/1/114)
- . 2010b, ApJ, 722, 1985, doi: [10.1088/0004-637X/722/2/1985](https://doi.org/10.1088/0004-637X/722/2/1985)
- Yu, S., & Jeffery, C. S. 2010, A&A, 521, A85, doi: [10.1051/0004-6361/201014827](https://doi.org/10.1051/0004-6361/201014827)

APPENDIX

A. DETECTION RATE NORMALISATION

In this section we explain in detail the normalisation process that we refer to in Section 2.3. From each instance of the Milky Way that we simulate we can extract the fraction of targets that are detectable, where we define a target as one of BHBH, BHNS or NSNS that merges in a Hubble time. Note that we complete this calculation separately for each DCO type and each model variations.

We now explain how to convert the detectable fraction to a detection rate for the Milky Way. We write that the *number* of detectable targets in the Milky Way is

$$N_{\text{detect}} = f_{\text{detect}} \cdot N_{\text{target,MW}}, \quad (\text{A1})$$

where f_{detect} is the fraction of targets in the instance that were detectable and $N_{\text{target,MW}}$ is the total number of targets that have been formed in the Milky Way's history. We can further break this total down into

$$N_{\text{target,MW}} = \langle \mathcal{R}_{\text{target}} \rangle \cdot M_{\text{SF,MW}}, \quad (\text{A2})$$

where $\langle \mathcal{R}_{\text{target}} \rangle$ is the average number of targets formed per star forming mass and $M_{\text{SF,MW}}$ is the star forming mass of the Milky Way, meaning the total mass of every star ever formed in the Milky Way. We explain how to calculate each of these terms in respective subsections below.

A.1. Average target formation rate

Double compact object formation is strongly metallicity dependent, so we must find the average rate as the integral over metallicity

$$\langle \mathcal{R}_{\text{target}} \rangle = \int_{Z_{\min}}^{Z_{\max}} p_Z \mathcal{R}_{\text{target},Z} dZ, \quad (\text{A3})$$

where Z_{\min} , Z_{\max} are the minimum and maximum sampled metallicities, p_Z is the probability of forming a star at the metallicity Z (which can be found using the distribution in Frankel et al. 2018) and $\mathcal{R}_{\text{target},Z}$ is the number of targets formed per star forming mass.

$$\mathcal{R}_{\text{target},Z} = \frac{N_{\text{target},Z}}{M_{\text{SF},Z}}. \quad (\text{A4})$$

In reality, this integral is instead approximated as a sum over the metallicity bins that we use in our simulation. The number of targets in our sample at a metallicity Z , $N_{\text{target},Z}$, can be written simply as the sum of the targets' weights:

$$N_{\text{target},Z} = \sum_{i=1}^{N_{\text{binaries},Z}} w_i \theta_{\text{target},i}, \quad (\text{A5})$$

where w_i is the adaptive importance sampling weight assigned to the binary by STROOPWAFEL, $N_{\text{binaries},Z}$ is the number of binaries at metallicity Z in our sample and $\theta_{\text{target},i}$ is a step function that is only 1 when the binary is a target and otherwise 0.

The total star forming mass at a metallicity Z , $M_{\text{SF},Z}$, can be written as

$$M_{\text{SF},Z} = \frac{\langle m \rangle_{\text{COMPAS},Z}}{f_{\text{trunc}}} \sum_{i=1}^{N_{\text{binaries},Z}} w_i, \quad (\text{A6})$$

where $\langle m \rangle_{\text{COMPAS}}$ is the average star forming mass of a binary in our sample and f_{trunc} is the fraction of the total stellar mass from which COMPAS samples, given its truncated mass and separation ranges (see Section 2.1). The cuts applied to the distributions, mainly because only massive stars are sampled, mean that only $f_{\text{trunc}} \approx 0.2$ of the stellar mass in the galaxy is sampled from.

A.2. Total star forming mass in the Milky Way

It is important to distinguish between the *total* mass of every star formed over the entire history of the Milky Way and the *current* stellar mass in the Milky Way. Many stars born in the Milky Way are no longer living and have lost much of their mass to stellar winds and supernovae, thus the current stellar mass in the Milky Way is an underestimate of the total star forming mass.

Licquia & Newman (2015) find that the total stellar mass today in the Milky Way is $6.08 \pm 1.14 \times 10^{10} M_{\odot}$. This total includes all stars and stellar remnants (white dwarfs, neutrons stars and black holes) but *excludes* brown dwarfs. We can write that the total mass of every star every formed in the Milky Way is

$$M_{\text{SF,MW}} = 6.08 \pm 1.14 \times 10^{10} M_{\odot} \cdot \frac{\langle m \rangle_{\text{SF,total}}}{\langle m \rangle_{\text{SF,today}}}, \quad (\text{A7})$$

where $\langle m \rangle_{\text{SF,total}}$ is the average mass of a star over the history of the Milky Way and is defined as

$$\langle m \rangle_{\text{SF,total}} = \int_0^{t_{\text{MW}}} p_{\text{birth}}(\tau) \int_{0.01}^{200} \zeta(m) m dm d\tau, \quad (\text{A8})$$

where t_{MW} is the age of the Milky Way, $\zeta(m)$ is the Kroupa (2001) IMF function and $p_{\text{birth}}(\tau)$ is the probability of a star being formed at a lookback time τ (Eq. 2). $\langle m \rangle_{\text{SF,today}}$ is the average mass of all stars and stellar remnants (excluding brown dwarfs) present in the Milky Way today is defined as follows (note that we integrate from 0.08 not 0.01 since observations of today's Milky Way mass exclude brown dwarfs)

$$\langle m \rangle_{\text{SF,today}} = \int_0^{t_{\text{MW}}} p_{\text{birth}}(\tau) \int_{0.08}^{200} \zeta(m) m_{\text{today}}(m, \langle Z \rangle_{\tau}, \tau) dm d\tau, \quad (\text{A9})$$

where $m_{\text{today}}(m, Z, \tau)$ is the current mass of a star that was formed τ years ago at a metallicity Z . We calculate $m_{\text{today}}(m, Z, \tau)$ by interpolating the final masses given by COMPAS for a grid of single stars over different masses and metallicities using the Fryer et al. (2012) delayed prescription and default wind mass loss settings. We only use the final mass if more than the main sequence lifetime of the star has passed, otherwise we just use the initial mass. Since we don't know the exact metallicity of each star we use the average star forming metallicity in the Milky Way at a lookback time τ using the birth radius distribution and metallicity equation from Frankel et al. (2018). If we now evaluate Equation A7, we find that the total mass of every star that has ever formed in the Milky Way is

$$M_{\text{SF,MW}} = 6.1 \pm 1.1 \times 10^{10} M_{\odot} \cdot \frac{0.384 M_{\odot}}{0.257 M_{\odot}} = 9.1 \pm 1.1 \times 10^{10} M_{\odot}, \quad (\text{A10})$$

an increase of approximately 50% from the value still in stars today!

A.3. Normalisation summary

Finally, we can substitute Equations A3 and A7 into A1 and write that the overall normalisation of the detection rate is calculated as

$$N_{\text{detect}} = f_{\text{detect}} \cdot 9.1 \times 10^{10} M_{\odot} \cdot \sum_{Z=Z_{\min}}^{Z_{\max}} p_Z \left(\sum_{i=1}^{N_{\text{binaries},Z}} w_i \theta_{\text{target},i} \right) \left(\frac{\langle m \rangle_{\text{COMPAS,Z}}}{f_{\text{trunc}}} \sum_{i=1}^{N_{\text{binaries},Z}} w_i \right)^{-1} \quad (\text{A11})$$

B. SUPPLEMENTARY MATERIAL

B.1. Detection rate table

B.2. Physics variation cumulative distributions

B.3. Formation channels

Table 2. The number of detectable binaries in a 4 and 10 year LISA mission for the 15 different model variations and each DCO type. Each value shows the median and the 90% confidence interval.

Model	LISA (4 year)			LISA (10 year)		
	BHBH	BHNS	NSNS	BHBH	BHNS	NSNS
A	34.4 ^{+46.6} _{-20.9}	29.9 ^{+47.4} _{-20.1}	7.7 ^{+10.3} _{-5.0}	58.6 ^{+53.3} _{-31.0}	51.9 ^{+95.0} _{-28.0}	13.0 ^{+14.2} _{-6.8}
B	33.9 ^{+36.5} _{-19.7}	15.5 ^{+19.6} _{-9.6}	2.8 ^{+4.3} _{-1.9}	55.6 ^{+45.9} _{-27.7}	26.7 ^{+23.7} _{-13.8}	4.8 ^{+5.6} _{-2.7}
C	20.6 ^{+20.5} _{-11.1}	5.3 ^{+5.3} _{-3.0}	4.3 ^{+5.2} _{-3.1}	33.7 ^{+26.7} _{-15.7}	8.9 ^{+7.0} _{-4.2}	7.3 ^{+6.1} _{-4.5}
D	21.9 ^{+37.8} _{-14.7}	4.1 ^{+4.2} _{-2.6}	11.6 ^{+22.7} _{-8.3}	36.0 ^{+45.4} _{-21.6}	6.8 ^{+5.3} _{-3.4}	20.5 ^{+27.7} _{-12.7}
E	33.7 ^{+37.0} _{-19.4}	3.3 ^{+6.3} _{-2.3}	0.2 ^{+0.1} _{-0.1}	54.9 ^{+44.2} _{-26.7}	5.8 ^{+8.2} _{-3.5}	0.3 ^{+0.2} _{-0.1}
F	26.2 ^{+35.8} _{-16.0}	15.0 ^{+84.0} _{-11.4}	5.7 ^{+7.3} _{-3.8}	43.3 ^{+43.7} _{-22.2}	27.2 ^{+86.3} _{-18.2}	9.5 ^{+10.0} _{-5.2}
G	29.5 ^{+27.6} _{-15.9}	23.5 ^{+27.2} _{-14.0}	23.4 ^{+27.9} _{-15.2}	47.5 ^{+38.3} _{-21.4}	40.9 ^{+36.3} _{-20.7}	39.8 ^{+36.3} _{-21.4}
H	115.1 ^{+123.0} _{-98.0}	30.7 ^{+163.7} _{-21.4}	7.4 ^{+14.6} _{-4.8}	173.6 ^{+150.5} _{-117.7}	55.4 ^{+185.8} _{-32.8}	13.0 ^{+25.5} _{-6.8}
I	22.7 ^{+26.8} _{-12.4}	48.7 ^{+97.1} _{-30.9}	6.3 ^{+9.0} _{-4.0}	36.1 ^{+30.8} _{-16.8}	84.0 ^{+142.8} _{-45.0}	10.9 ^{+11.1} _{-5.8}
J	47.5 ^{+71.9} _{-31.6}	24.3 ^{+37.4} _{-16.3}	6.8 ^{+10.9} _{-4.4}	80.7 ^{+86.8} _{-46.8}	41.7 ^{+47.0} _{-22.9}	11.6 ^{+14.0} _{-6.2}
K	30.1 ^{+40.4} _{-18.0}	37.6 ^{+44.9} _{-24.6}	7.8 ^{+11.6} _{-5.1}	52.5 ^{+48.4} _{-28.2}	65.1 ^{+54.7} _{-35.0}	13.4 ^{+14.8} _{-7.1}
L	35.2 ^{+45.2} _{-21.3}	30.2 ^{+49.6} _{-19.9}	7.9 ^{+11.7} _{-5.0}	58.9 ^{+54.9} _{-31.0}	52.4 ^{+96.9} _{-28.5}	13.3 ^{+14.8} _{-7.1}
M	43.0 ^{+58.3} _{-28.3}	68.7 ^{+108.7} _{-43.4}	16.1 ^{+20.5} _{-10.4}	69.4 ^{+69.1} _{-38.1}	117.4 ^{+154.5} _{-61.8}	27.3 ^{+26.4} _{-14.5}
N	53.0 ^{+58.3} _{-34.1}	110.6 ^{+193.1} _{-71.3}	35.7 ^{+54.8} _{-23.6}	84.4 ^{+73.3} _{-44.9}	194.9 ^{+256.0} _{-102.6}	60.2 ^{+67.8} _{-32.7}
O	43.1 ^{+39.0} _{-27.0}	76.0 ^{+91.2} _{-43.9}	9.3 ^{+10.4} _{-6.0}	68.5 ^{+47.5} _{-35.8}	130.8 ^{+122.0} _{-62.9}	15.8 ^{+13.8} _{-8.4}
P	44.3 ^{+62.2} _{-28.4}	26.7 ^{+48.9} _{-17.0}	9.0 ^{+10.9} _{-5.6}	69.9 ^{+78.9} _{-38.0}	45.9 ^{+64.4} _{-25.9}	15.3 ^{+13.9} _{-7.4}
Q	0.0 ^{+0.0} _{-0.0}	6.3 ^{+6.1} _{-3.7}	7.8 ^{+8.0} _{-4.7}	0.0 ^{+0.0} _{-0.0}	10.8 ^{+7.6} _{-5.3}	13.0 ^{+10.4} _{-6.4}

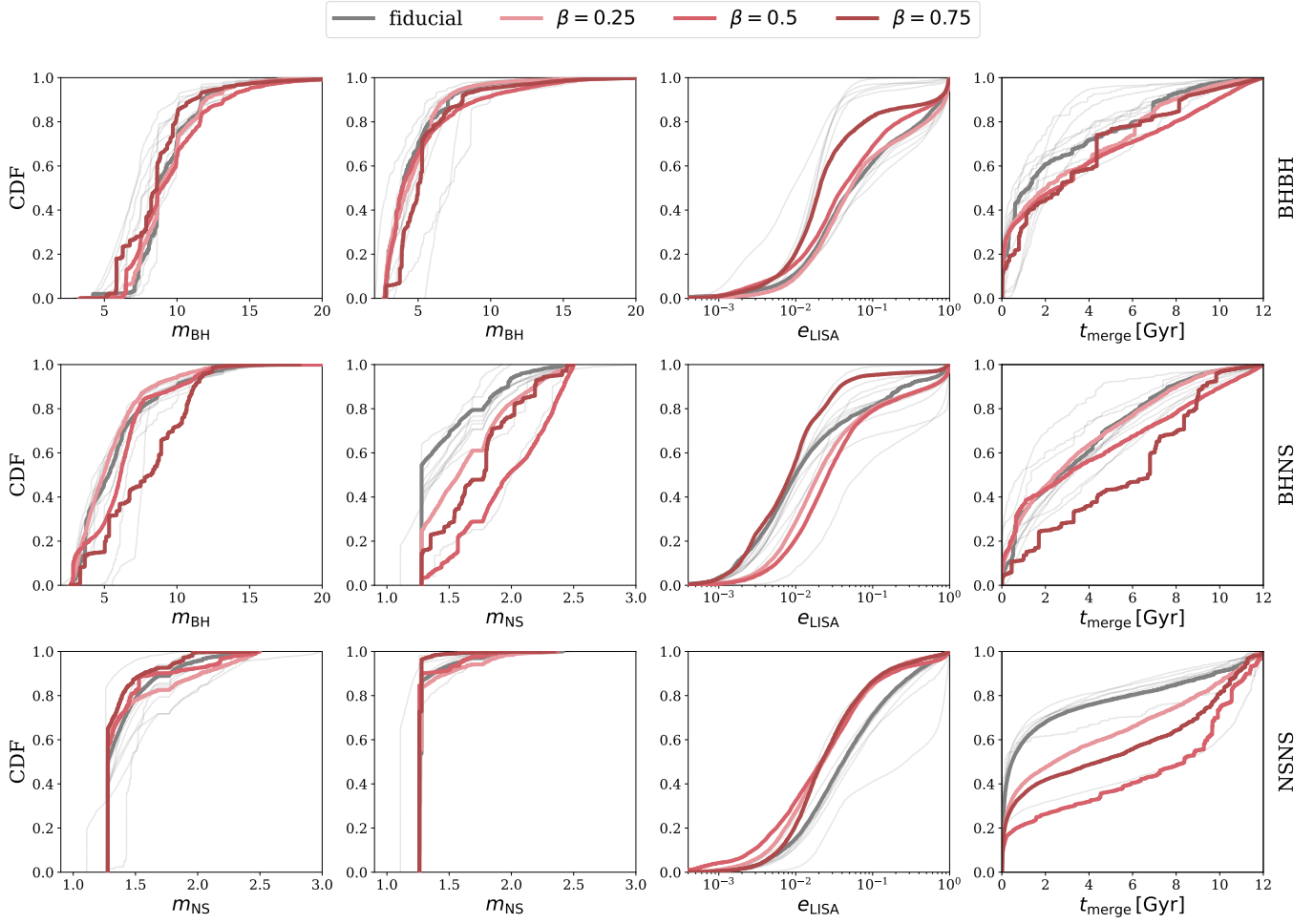


Figure 6. Cumulative distribution functions for the black hole mass, neutron star mass, eccentricity during the LISA mission and merger time for each DCO type and physics variation. In colour we show the fiducial populations compared to changing the mass transfer efficiency β . We additionally show the other physics variations in the background in light grey.

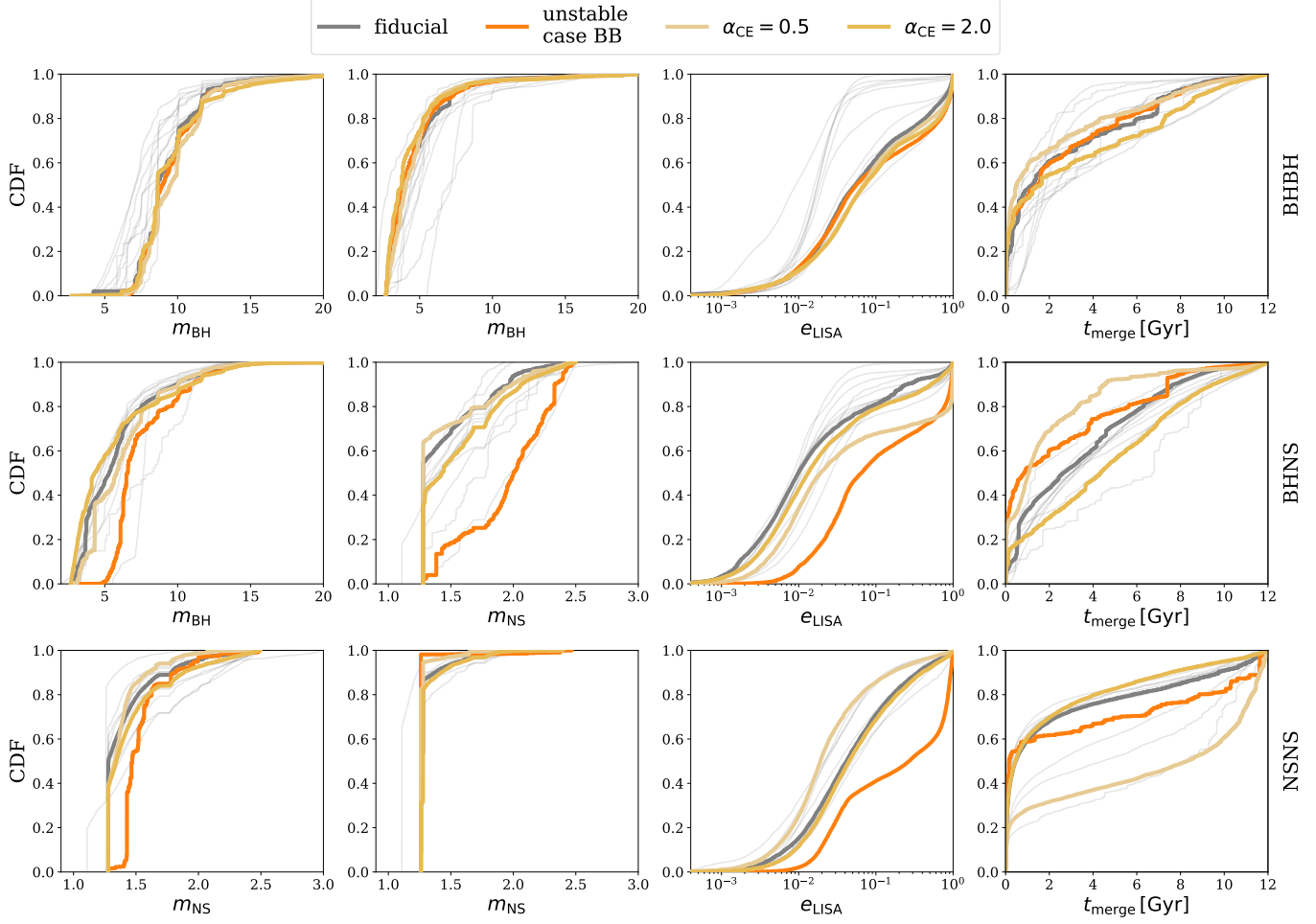


Figure 7. As Fig. 6, except comparing the fiducial population with models using different values for α_{CE} and changing the stability of case BB mass transfer.

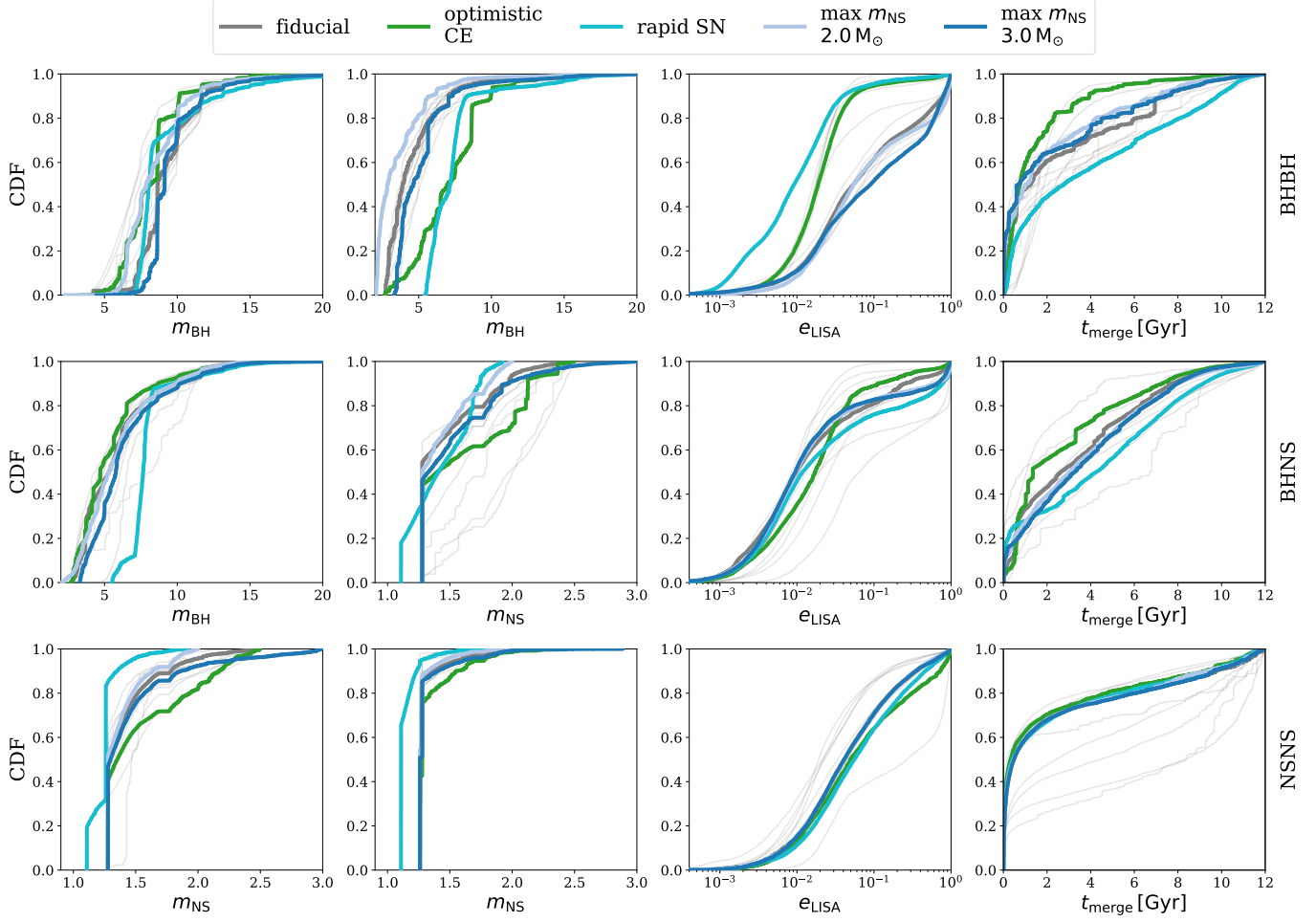


Figure 8. As Fig. 6, except comparing the fiducial population with models changing the maximum neutron star mass, remnant mass prescription and survivability of common envelope events initiated by Hertzsprung gap donors.

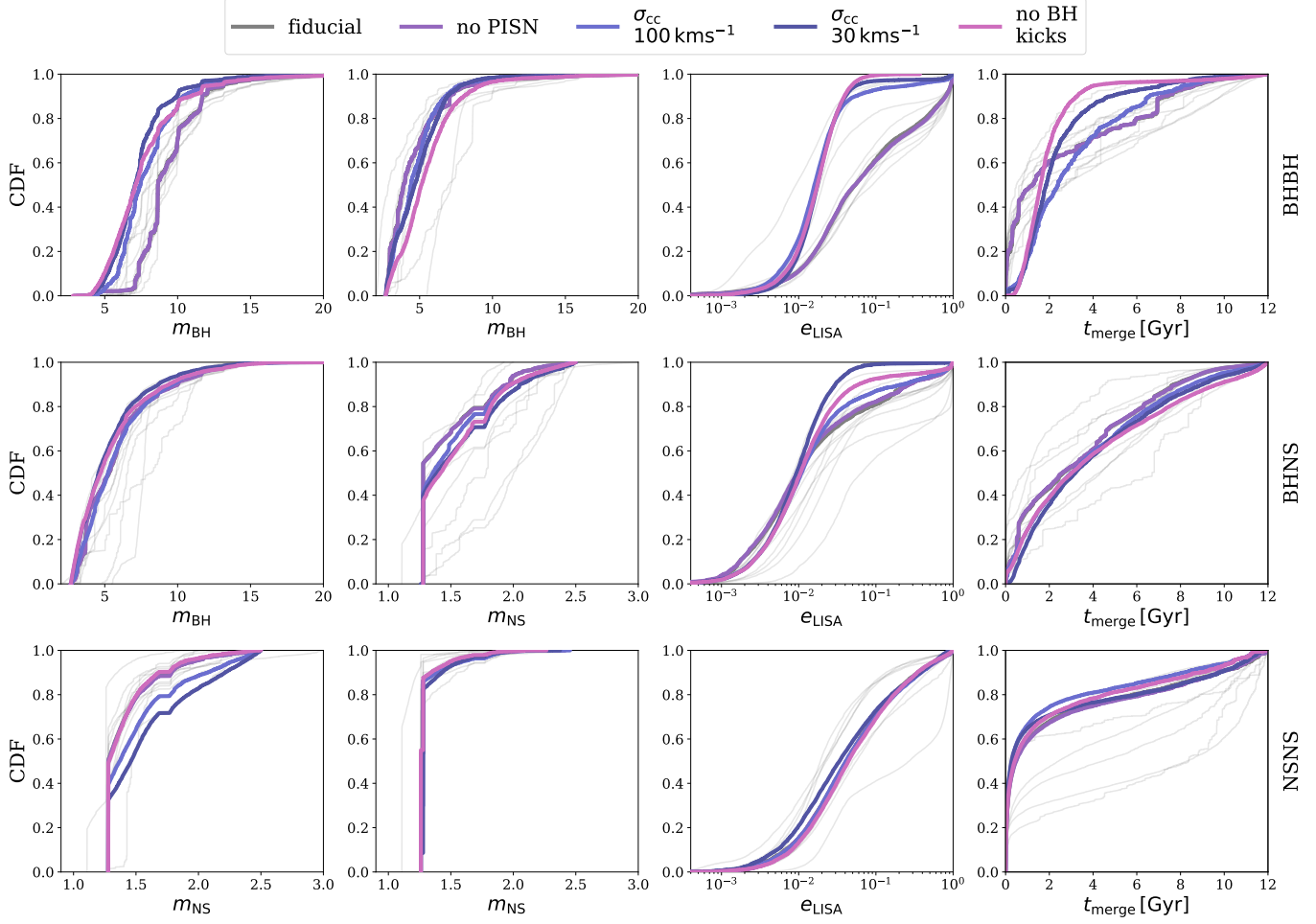


Figure 9. As Fig. 6, except comparing the fiducial population with models changing the core-collapse supernova kick distributions and the presence of BH kicks and PISNs.

